GROWTH AND PROPERTIES OF DIAMOND AND DIAMOND-LIKE MATERIALS

Markus Kaukonen

Laboratory of Physics
Helsinki University of Technology
02150 Espoo, Finland

ESPOO 1999

GROWTH AND PROPERTIES OF DIAMOND AND DIAMOND-LIKE MATERIALS

Markus Kaukonen

Laboratory of Physics
Helsinki University of Technology
02150 Espoo, Finland

Dissertation for the degree of Doctor of Technology to be presented with due permission for public examination and debate in Auditorium E at Helsinki University of Technology (Espoo, Finland) on the 10th of December, 1999, at 12 o'clock noon.

Abstract

Based on modeling and simulation, a new interpretation of the growth of amorphous carbon (*a-C*) is proposed. The growth is shown to proceed both on the surface and in the subsurface regions depending on the kinetic energy of the incident ion beam. Co-deposition with inert ions is recommended. For chemical vapor deposition (CVD) growth with nitrogen doping, a new growth mechanism is revealed. This enables direct insertion of the gas phase molecule C_2H_2 (ethyne) on the growing diamond 100 surface, without preceding hydrogen abstraction reactions. The doping of diamond and *a-C* with nitrogen (N), oxygen (O) and chlorine (Cl) is studied. Among these atom species nitrogen has the lowest formation energy, *i.e.* it is most easily soluble into diamond or *a-C* from the gas phase. The substitutional N is found to be an active dopant only when located on the surface of *a-C*. This explains the low doping efficiency for *a-C*. Furthermore, experimentally it is found that the minimum in the electron affinity of the N doped *a-C* films occurs at 0.4 % N doping concentration. This result is explained in this work in terms of the surface geometry of N atoms on the *a-C* surface.

Dissertations of Laboratory of Physics, Helsinki University of Technology
ISSN-1455-1802

Dissertation 108 (1999)
Markus Kaukonen: Growth and Properties of Diamond and Diamond-like Materials
ISBN 951-22-4780-1

LIBELLA PAINOPALVELU OY
ESPOO, 1999

Preface

This thesis has been prepared in the Laboratory of Physics at the Helsinki University of Technology during the years 1995-1999.

I would like to thank my supervisor Prof. Risto Nieminen for introducing me to the field of computational physics, and the support and ideas he gave me when carrying out the research. I thank my co-worker in the experimental side, Dr. Jari Koskinen. Furthermore I thank my German, English and Finnish collaborators Prof. Thomas Frauenheim, Dr. Paul Sitch, Dr. Gerd Jungnickel, Dr. Sylke Uhlmann, M. Sc. Michael Sternberg, M. Sc. Ari P. Seitsonen, Dr. Sami Pöykkö and Prof. Martti Puska from both scientific and human points of view.

I acknowledge the financial support from the Vaisala Foundation, and Center for Scientific Computing for generous computer resources.

Finally I thank Essi who even agreed on marriage during this work.

Espoo, August 1999

Markus Kaukonen

Contents

List of publications

This thesis consists of an overview and the following publications:

1. J.-P. Hirvonen, J. Koskinen, M. Kaukonen and R. M. Nieminen, *Dynamic relaxation properties of hard carbon films,* J. Appl. Phys. **81** 7248 (1997).

2. S. Pöykkö, M. Kaukonen, M. J. Puska and R. M. Nieminen, *Possible n-type dopants in diamond and amorphous carbon,* Comp. Mat. Science **10**, 351 (1998).

3. P. K. Sitch, G. Jungnickel, M. Kaukonen, D. Porezag, M. Pederson, K. A. Jackson and Th. Frauenheim, *A study of substitutional nitrogen impurities in chemical vapor deposited diamond,* J. Appl. Phys. **83**, 4642 (1998).

4. M. Kaukonen, P. K. Sitch, G. Jungnickel, D. Porezag, R. M. Nieminen and Th. Frauenheim, *Effect of N and B doping on the growth of CVD diamond (100):H(2x1) surfaces,* Physical Review B **57**, 9965 (1998).

5. M. Kaukonen, A. Seitsonen, S. Pöykkö, and R. M. Nieminen, *Nitrogen doping of amorphous carbon surfaces,* submitted to Physical Review Letters.

6. M. Kaukonen and R. M. Nieminen, *Atomic-scale modeling of the ion-beam-induced growth of amorphous carbon,* accepted to Physical Review B.

The author has had an active role in all phases of the research reported in this thesis. He has been involved in the planning of the calculations, the development of the computer programs, and the interpretation of the results. The author has written Publications 4, 5 and 6, and contributed actively to the writing of the other papers. He has been responsible for the development of the computer programs needed in Publications 1, 4, 5 and 6 and he is responsible of most of the calculations described in Publications 4, 5 and 6, and part of the calculations in Publication 1, 2 and 3.

Additionally the following classical or density-functional based tight-binding studies have been published during this work, or are near publishing:

M. Kaukonen and R. Nieminen, *The growth of diamond-like films,* Surf. Sci. **331**, 975 (1995).

J. Elsner, M. Kaukonen, M. I. Heggie, M. Haugk, Th. Frauenheim, and R. Jones, *Domain boundaries on $11\bar{2}0$ planes in GaN: A theoretical study,* Physical Review B **58**, 15347 (1998).

R. Astala, M. Kaukonen, T. Heine, and R. M. Nieminen, *Nanoindentation of silicon surfaces,* accepted to Physical Review B.

M. Kaukonen, G. Jungnickel, J. Peräjoki, Th. Frauenheim, and R. M. Nieminen, *Lattice independent Monte Carlo (LIMC) method for long time scale simulations,* accepted to Physical Review B.

1 Introduction

Diamond is a unique material. Its electronic structure ($1s^2 2s^2 2p^2$) is such that the formation of a very strong linear combination of the $2s$ and $2p$ electrons, *i.e.* sp^3, is energetically favored. Moreover, the energy gain in such a hybridization (for the process $2s^2\ 2p^2 \rightarrow sp^3$) is bigger than for any other atomic system. In naturally grown diamond, the carbon atoms have been exposed to high pressure and temperature for millions of years. Man has succeeded in copying nature by producing high-pressure high-temperature artificial diamond in laboratories. The vast energy needed in this artificial production has made it economically infeasible. Other methods for producing artificial diamond or diamond-like materials have been introduced. The commercially most successful technique has been that of chemical vapor deposition (CVD). The quality, however, of this kind of diamond is inferior to natural diamond due to point and other types of defects present. When giving up the requirement of repeating nature completely but achieving most of the properties of diamond, one obtains amorphous carbon (*a-C*), which at the atomic level may contain up to 80% diamond (*i.e.* sp^3) bonds. *a-C* is, for example, manufactured by extracting carbon atoms with a laser from a graphite target guiding the abstracted carbon atoms or molecules to a silicon substrate.

The growth of CVD-diamond and amorphous carbon leaves many open questions. What are the relevant chemical processes on the growing CVD-diamond surface? What is the role of doping in these processes? The existing atom-level models of the growth of amorphous carbon are lacking both computational and experimental evidence, with even the atomic and electronic structure of this material remaining uncertain. Further, extensive use of CVD-diamond or *a-C* in semiconductors has proved, as yet, impossible, since the donor-type (*i.e.* n-type) doping of these materials has not succeeded.

In this work, growth processes relevant to the chemical vapor deposited (CVD) diamond and amorphous carbon (*a-C*) have been studied using classical and tight-binding methods (Publications 4 and 6). Properties of single substitutional defects or excessive doping in diamond and *a-C* has been investigated applying tight-binding and *ab initio* techniques (Publications 2, 3 and 5). Macroscopical properties of *a-C* have been evaluated comparing molecular dynamics simulations using a classical potential with experimental characterizations (Publication 1).

The choice of the particular computational method has been made based on the system size and the relevant time scale of the simulation. The growth simulations of a-C with more than 1000 atoms, spanning in real time more than one ns (10^{-9} s), have been carried out with the empirical Tersoff potential. Diffusion on diamond surfaces with subsurface doping has been simulated applying molecular dynamics and the density-functional based tight-binding (DFTB) scheme. In this case the system size is of the order of 200 atoms, and instead of the true time evolution of the system, a semi-static approach in the simulation of diffusion events is applied. In the *ab initio* calculations the systems of the order of 100 atoms have been relaxed using direct energy functional minimization techniques.

The summary part of this thesis is organized as follows. An overview of the general properties of carbon-based materials is given in Sec. 2. Some fabrication methods of diamond and diamond-like materials are introduced in Sec. 3. The computational framework applied is presented in Sec 4. The results obtained in this thesis are discussed in Sec. 5, including both CVD-diamond and amorphous carbon. A brief summary is given in Section 6.

2 Carbon-based materials

In this section the vast variety of the pure carbon-based materials is briefly overviewed. The atomic and electronic arrangement of the different materials are described, followed by the macroscopically observable properties. This description is limited to pure carbon structures, excluding for example hydrocarbons, the basis of all living creatures.

2.1 Microscopic properties

A carbon atom has six electrons. Two of the electrons locate near the atom nucleus and do not participate in chemical bonding. The four uppermost electrons in energy are called valence electrons. They are located on average further away from the nucleus compared to the two core electrons. The valence electrons participate in chemical bonding. They lie so close to each other in energy that all or some of these electronic states can interact with each other and form linear combinations of their single electron wave functions. The possible linear combinations are called sp^1, sp^2 and sp^3. sp^1 bonding is present in linear carbon chains. Two electrons per atom are localized along the bond direction (σ-bonding) and two of them are localized in an orbital perpendicular to the bond direction (π-bonding). In graphite one has planar sp^2-bonding. Three of the four valence electrons of carbon are in σ-bonds, whereas the fourth is on a π-orbital. Diamond consists entirely of sp^3 bonded atoms and all the electrons are localized to the bond direction (σ-bonding). All the bonding combinations of carbon are sketched in Fig. 1.

The symbols for the anti-bonding orbitals in carbon are σ^* and π^*. With the bonding orbitals σ and π, the sum of single orbitals making the bond $|\phi_1 + \phi_2|^2$ is greater in amplitude between the atoms than with the anti-bonding ones $|\phi_1 - \phi_2|^2$. The magnetic interactions are neglected in this work, so each electron state has two electrons (this degeneracy is labeled as spin degeneracy).

Amorphous carbon (*a-C*) consists of a mixture of all the bonding types. A comprehensive review article about *a-C* written by Robertson is recommended for reading [1]. An example of a computer generated *a-C* surface is depicted in Fig. 2.

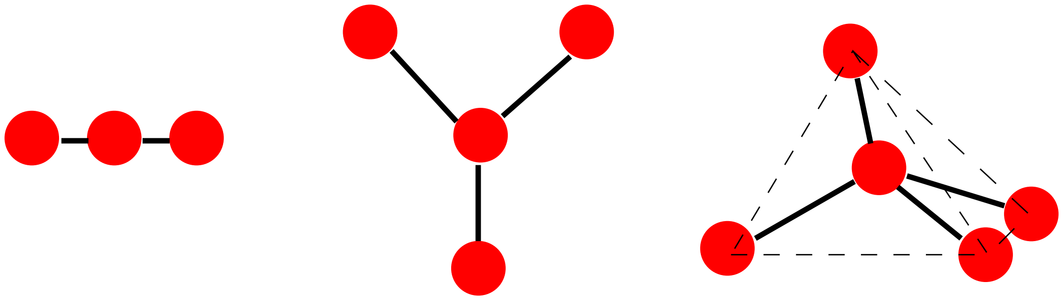

a) b) c)

Figure 1: The variety of the carbon bonds enables the vast number of different carbon-based materials and structures (such as humans). The bonding types are here shown schematically. a) The linear sp^1-bonds are present in linear chains or hydrocarbons. The π bond is not shown. b) The planar sp^2-bonds are present in graphite and in amorphous carbon. The π-bond is not shown. c) The three dimensional sp^3 bond exists in diamond and in amorphous carbon.

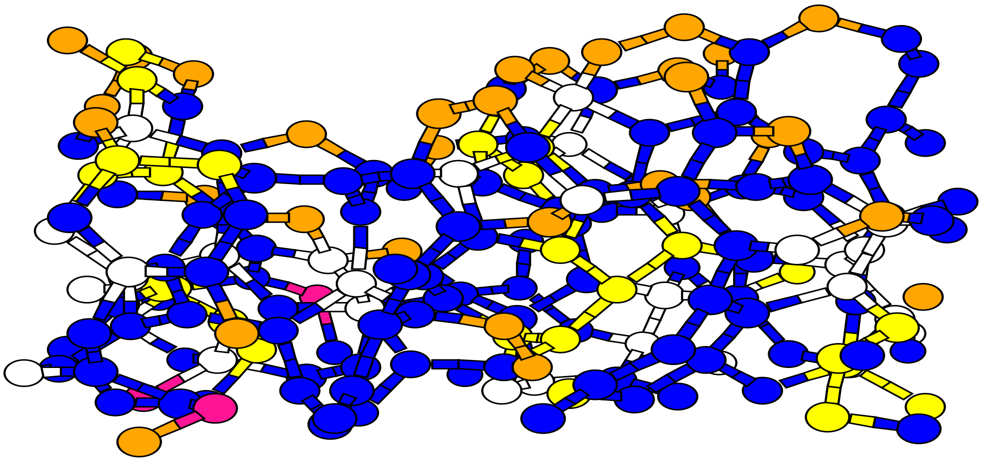

Figure 2: Amorphous carbon (a-C) consists of a mixture of all the bonding types. Here is an example of a simulated a-C surface grown with an atom-beam consisting of single carbon atoms with a kinetic energy of 150 eV. The different bonding types of atoms are indicated with different darkness. The sp^3 atoms are the white ones and the sp^2 atoms are the darkest ones.

It has been noticed that in *a-C* atoms with the same coordination number (*i.e.* the number of nearest neighbors) tend to cluster. The three-fold coordinated (sp^2-like) atoms are marked with the darkest color. This is because similar atoms are able to combine their similar atomic orbitals with maximal overlap. A model for the electronic density of states has been proposed by Robertson [2]. The energy of the electron states in his model is given as

$$E_n = 2\beta cos(\frac{2\pi n}{N}), n = 1, 2, 3, ..., N, \tag{1}$$

where N is the number of atoms in a carbon chain or ring. The energy levels are obtained by solving the Schrödinger equation using only nearest-neighbor interactions and a parameterized value β for the expectation value of the Hamiltonian between nearest-neighbor orbitals ϕ_i and ϕ_j, *i.e.* $\beta = < \phi_i|H|\phi_j >$. Thus the energy gap with even number of electrons is

$$E_{gap} = \frac{2\beta\pi}{N} \tag{2}$$

When fusing the stablest rings (6-rings) together, Robertson obtains (M being the number of 6-rings in the cluster)

$$E_{gap} = \frac{2|\beta|}{\sqrt{M}}. \tag{3}$$

This model explains qualitatively the gap size of small carbon molecules up to graphite (in graphite N $\Rightarrow \infty \Rightarrow E_{gap} = 0.0$). The gap is between π and π^* because the π levels are higher in energy compared to the σ levels. Based on this reasoning, Robertson suggests that *a-C* consists of graphitic domains with dimension 15-20 Å of sp^2 bonded clusters, having 35-60 6-rings leading to his experimental E_{gap} = 0.4-0.7 eV.

On the contrary, graphite is a semi-metal with a low density of electronic states at the Fermi level. Weak conduction takes place in the direction of the graphite planes. Diamond is an insulator with a large indirect energy gap of 5.5 eV (*i.e.* the lowest energy transition requires a change in the electron momentum). The electronic densities of states of the carbon-based materials are schematically depicted in Fig. 3. Only the Γ-point ($\mathbf{k} = 0$) is used for the Brillouin-zone sampling (see Sec. 4.3). This is adequate, because there is no long-range periodicity in the amorphous system.

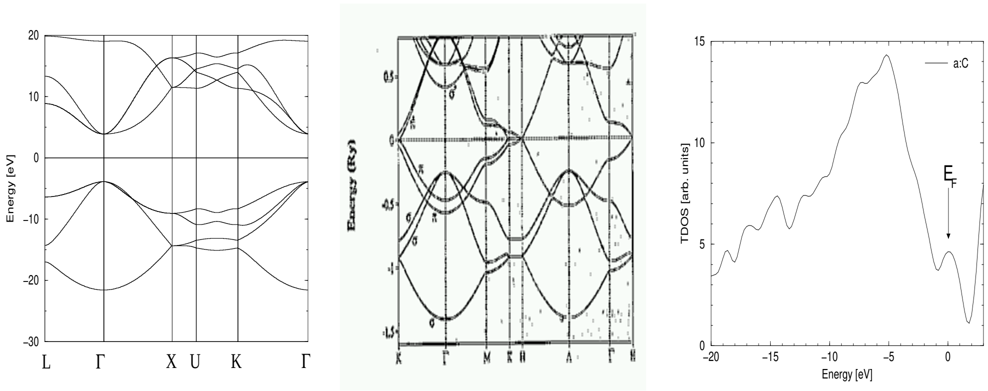

(a) Diamond (b) Graphite (c) *a-C*

Figure 3: a) The band structure of diamond is calculated using the DFTB-method (Sec. 4.2). The valence band is correctly represented. b) Graphite doesn't possess a band gap, so it is a semi-metal. The conductivity takes place only along the graphitic planes. The picture is taken from Ref. [3]. c) A band gap of the order of 2 eV is measured experimentally in amorphous carbon (*a-C*). However, in the DFT-LDA calculations there is no electronic gap. The figure is from Publication 5.

Another view to the structure of *a-C* is given by Stephan et al. [4]. Their calculations are based on atom-scale simulations using a density-functional based tight-binding (DFTB) method (Sec. 4.2). They consider the Robertson picture as oversimplified, because they find no clear graphitic domains in *a-C*. At the stablest density (*i.e.* energy per atom is at its minimum) of ρ 3.0 $\frac{g}{cm^3}$, *a-C* consists roughly two thirds of 4-fold atoms (sp^3), the rest being 3-fold (sp^2) coordinated. The sp^2 and sp^3 atoms form rings, but these rings consist of both sp^2 and sp^3 bonded atoms. Any fully π-bonded rings are not found (such as one has in graphite), in contrast to the Robertson model. The sp^2-like atoms tend to cluster with even number of atoms: almost all sp^2 atoms are paired at 3.0 $\frac{g}{cm^3}$. The electronic structure has no gap. The gap-filling states stem from isolated sp^2 atoms with only sp^3 neighbors. Also sp^2 chains with odd number of atoms result in states in the gap. These gap states are localized at the end of the sp^2 chain. Isolated sp^1 atoms (if present) would also give rise to defect states in the gap. When seriously distorted from the ideal diamond geometry (bond length $\sim$ 1.54 Å, bond angle $\sim$ 109°), the distorted sp^3 orbitals may interact with neighboring atomic orbitals resulting in some electron state density to the gap region. However, the density of states of the distorted sp^3 atoms is low compared to the other gap states.

In *ab initio* studies, on the contrary to the classical or tight-binding calculations, three and four membered carbon rings are present in a-C [5, 6]. These do not, however, contribute any electronic states to the gap.

Doping means the existence of unoccupied electron levels in the vicinity of the valence band (p-type doping) or occupied states near the edge of the conduction band (n-type doping). One can excite electrons thermally or by other means from the valence band to the previously unoccupied p doping level, leaving a lack of one electron, a 'hole', in the valence band. Only the electron levels that are not fully occupied and that are sufficiently delocalized can carry electric current. Thus creating a 'hole' in the valence band enables a current to flow. Similarly an electron from a previously occupied n-type doping level can be thermally excited to the conduction band. Again a partly occupied level, the continuum of conduction band levels, can carry a current. Substituting one C atom in diamond (all atoms sp^3) with an atom with one more (for example nitrogen, N) or one less (boron, B) electron in the outermost electron shell leads to the creation of a doping level. Boron substitution yields an unoccupied state 0.4 eV above the edge of the valence band. Nitrogen substitution in diamond at a sp^3 site would result an occupied n-type doping level approximately 0.2 eV below the conduction band. The formation of the doping levels can be understood based on the diagram presented in Fig. 4.

Taking one carbon atom away from a perfect diamond lattice leaves four floating orbitals which can be thought to correspond to the s and p levels [7] of a carbon atom. These floating orbitals combine with the atomic levels of the substitute atom. The electron orbitals formed by this combination are filled with the available number of electrons, *i.e.* four electrons from the neighboring C atoms and five from N or three from B. The single nitrogen substitution in diamond gives raise to two nitrogen-related bonding states in the valence band (with two and six electrons due to the degeneracy), and one singly occupied anti-bonding state 0.2 eV below the conduction band edge (Fig. 4). For boron there are two electrons less compared to nitrogen. Thus the highest occupied orbital is the combination of p-states with five electrons (Fig. 4). Because the electron energies of a free boron atom are higher in energy compared to nitrogen and carbon, this state with five electrons lies now 0.4 eV above the edge of the valence band. This state

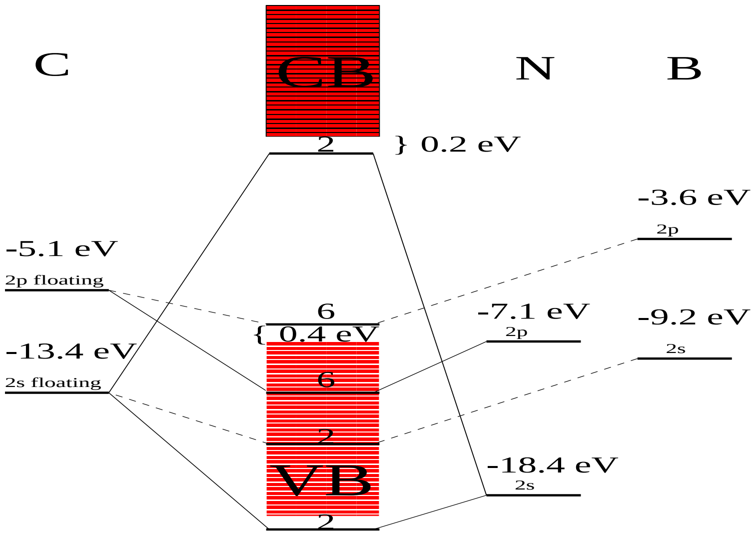

Figure 4: The floating carbon orbitals at a carbon vacancy (left) are saturated with the orbitals of the substitute atom N or B (right). These combinations of nearly-atom orbitals yield the final impurity related states (middle). The nitrogen related states are indicated by solid lines and the boron related states with dotted lines.

is missing one electron, so one has p-type doping. The possible doping sites for nitrogen in a-C (n-type doping) are sketched on the lower row in Fig. 5. As can be seen, a weakly bonded electron must be present in order to obtain doping.

If this would be the whole story, diamond could easily be both n- and p-doped. In reality diamond can only be p-doped but not n-doped. This is because the N atom does not stay in the sp^3 configuration, but a structural relaxation follows. One of the four sp^3 bonds breaks and the N atom ends up with a configuration with three electrons in single bonds to neighboring three C atoms and two electrons remain near the N atom in a non-bonding, so-called lone-pair state. The resulting configuration does not produce p- or n- type doping, but an occupied lone-pair state on the top of the valence band, and one unoccupied mid-gap state (associated with the broken bond on the neighboring C atom) [8]. Other n-dopants than nitrogen have larger formation energies in diamond and in a-C, *i.e.* it is difficult to incorporate them into the material [9]. However, there is recent experimental evidence in favor of the n-type doping in diamond using phosphorus [10]. A lone-pair defect in the same figure (Fig. 5) is not a doping configuration, because a

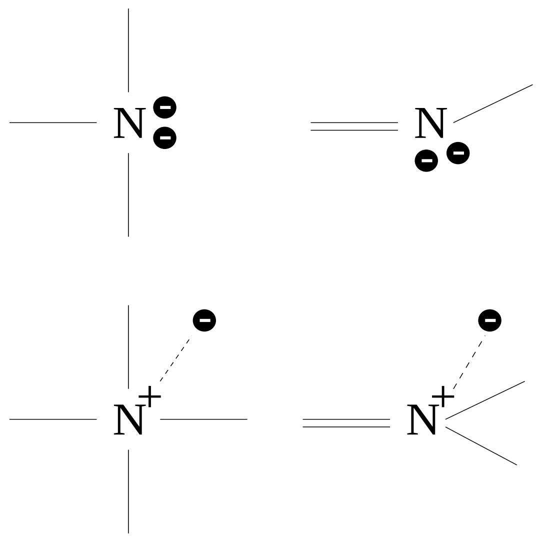

Figure 5: Upper row: Non-doping configurations with a localized lone-pair of electrons resulting in a state in the valence band. Lower row: Doping configurations causing a weakly localized state near the edge of the conduction band.

lone-pair state is in the valence band and it is localized at the N atom.

In bulk *a-C* N prefers substitutional sp^2 sites [9, 11]. The electron states associated to N are most commonly in the valence band or near it in the gap, because of the sp^2 and a lone-pair electron configuration. As in diamond, carbon-defect-related mid-gap states may arise if the N substitution causes dangling bonds to carbon atoms in its neighborhood. However, near the surface of *a-C* the nitrogen atom prefers initially a sp^3 site which then turns to sp^2 and a lone-pair (Publication 5). Furthermore, even if one in some bonding configurations would be able to create electrons states near the conduction band edge, the electrons would escape to lower lying localized and non-doping π^* states in sp^2 chains, as found by Stephan [4]. The control of the distribution of the π and π^* states in energy is at present experimentally impossible, *i.e.* one cannot design the distribution of the lengths of the π-bonded sp^2 chains.

Because of the difficulties in n-doping described above, Jungnickel *et al.* [12] have used a different approach. They have computer generated materials consisting only of 8-membered carbon rings. These materials are indeed n-dopable, and their material properties are near to diamond (hardness, chemical stability, etc.). It remains to be seen whether these materials

Table 1: Macroscopical and mechanical properties of diamond, graphite and a-C [13, 14, 15, 16]. Symbols used in the table are: ρ is density, H is Vicker's hardness, E is Young's modulus, λ is thermal conductivity at 300 K and μ_e is the electron mobility at 300 K. Dia is diamond, gra is graphite and a-C is amorphous carbon. Young's modulus for graphite is along the graphite plane direction.

	ρ [$\frac{g}{cm^3}$]	sp^3 [%]	Gap [eV]	H [GPa]	E [GPa]	λ [$\frac{W}{cmK}$]	μ_e [$\frac{cm^2}{Vs}$]
Dia	3.515	100	5.5	103	1050	10-25	2150
Gra	2.267	0	≈ 0	-	686	-	-
a-C	2.267	0	0.4 - 2.6	15-110	140-1000	-	-

can be produced in reality, because carbon 6-membered-rings are slightly more energetically favorable compared to 8-membered-rings.

2.2 Macroscopic properties and applications of carbon-based materials

Diamond and a-C are chemically inert and resistant against radiation damage. They have high Young's modulus and hardness. Diamond has the highest thermal conductivity and the highest electron mobility of all semiconductors at elevated temperatures. The general properties of diamond and a-C are summarized in Tab. 1.

The phase diagram of carbon is presented in Fig. 6. It can be seen that diamond is formed at high pressures and temperatures. Graphite is the stablest form of carbon at everyday conditions. This diagram presupposes thermal equilibrium, which means that the velocity distribution of the C atoms and the occupation distribution of the electronic states follow a well-defined statistical distribution at a given temperature. However, one can grow artificial diamond films also in non-equilibrium conditions using for example chemical vapor deposition (CVD) or other methods (Sec. 3). The non-equilibrium conditions enable diamond growth even outside of the diamond region in the phase diagram.

The superior properties of diamond and a-C can be realized in practical applications. Hard coatings in industry or in medical applications are in use already today. The main problem in this field is the attachment of the diamond-like coating to various materials to be coated. In most cases

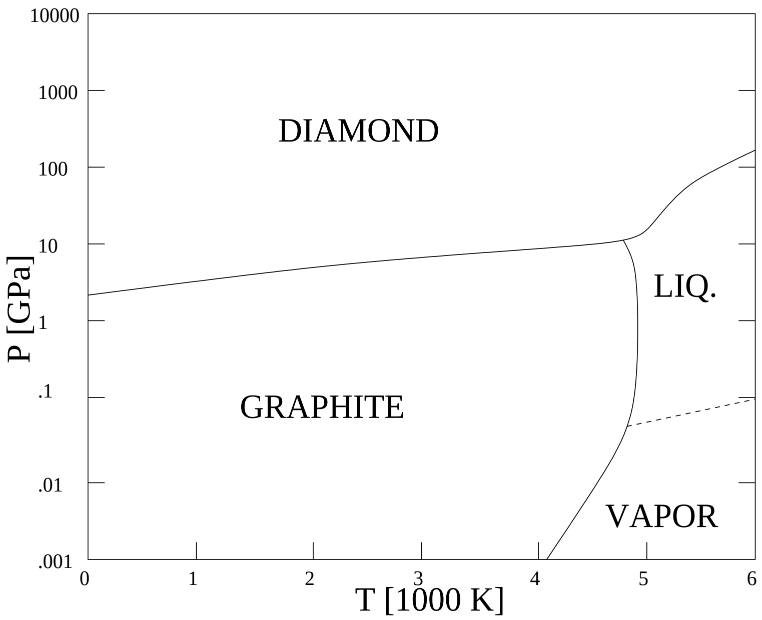

Figure 6: The phase diagram of carbon according to Bundy [17]. The nature of the liquid phase of a-C (LIQ. in the figure) is explained by Galli *et al.* [18].

cleanliness of the surface and chemical pre-treatments are necessary for durable coatings.

Diamond windows are also currently in use. Because of its large electronic gap (5.5 eV), diamond is transparent to light from ultra-violet to infra-red. These windows are used to protect vulnerable detectors, or they may be used as transparent material in extreme conditions, such as in space applications.

Diamond heat-spreaders have been commercially applied. Because diamond has the largest thermal conductivity and very low thermal expansion coefficient [1.05 $\frac{pm}{K}$] it has been used to conduct heat from for example laser diodes. However, diamond has a low heat capacity [16], so it can be used to conduct but not to store heat.

Boron-doped diamond can be used as heat sensor in harsh environments. The boron acceptor level lies about 0.4 eV above the valence band maximum (VBM), so at room temperature only a small fraction of electrons are excited to this level ($k_bT \approx 0.01$ eV at 300 K). Elevating the temperature increases the number of current carriers exponentially, and thus by measuring current one can infer temperature.

Pressure or acceleration censors base their functioning on the piezoresistance effect. When B-doped diamond is strained the position of the p-doping level changes with respect to the VBM. This occurs because the B-C bonds get shorter or longer due to the strain. When the bonds elongate the B atom becomes more free-atom-like. This causes the boron-associated electron level move further away from the VBM. The compressive stress causes an opposite effect [16]. Again, the change in the position of the level yields an exponential change in the current.

Diamond diodes and transistors should outperform current semiconductor devices. This is because of the high carrier mobility (Tab. 1) and high breakdown voltage (meaning that the diamond transistor could operate over a large voltage range). In practice results in this field have been poor. This is mainly because the failure in n-type doping of diamond or a-C (Sec. 2.1). Some Schottky diodes for scientific purposes have been made with operating temperatures of 300 °C - 1000 °C [19].

Field emission from a-C has been examined intensively in the last few years [20, 14]. Diamond-like surfaces have low or even negative electron affinity, meaning that electrons in a-C can be extracted to vacuum easily using a low electric field. The extracted electrons are accelerated and collided to phosphor pixels on a flat screen. The screen may be in practice a part of a flat computer or a television set. The physics of field emission in a-C is currently not well understood. In Publication 5 we propose that nitrogen doping of a-C films changes the dipole moment of the surface in such a way that the work function is decreased and thus the field emission is enhanced. On the other hand, it is suggested that large graphitic domains on the surface of a-C are responsible for the electron emission of a-C films.

a-C solar cells have been fabricated recently [21]. Nitrogen doped a-C is deposited on a Si substrate. The creation of electron-hole pairs when shining light on this device has been reported, with photo-currents of the order of 5 $\frac{mA}{cm^2}$ being measured.

Recently Gerstner and McKenzie have demonstrated the possibility of making memory elements of nitrogen-doped a-C [22]. Applying a bias voltage they are able to turn the memory element 'ON' or 'OFF'. In the 'ON' state the electrons in the energy gap are excited by a bias voltage to donor states. When the bias voltage is turned off, the electrons are trapped to the donor states and the sample conducts current. In the 'OFF' state a reverse bias voltage is applied and the states near conduction band become empty. Thus no current flows after the reverse bias pulse, and the device is in the 'OFF' state. Whether these devices can be manufactured in practice on a large scale remains an open question. This is because the precise control of the distribution of the electronic states in the a-C band gap is currently impossible (Sec. 2.1).

3 Fabrication and analysis of diamond and diamond-like materials

In this section a brief description of the most commonly used methods to produce artificial diamond or amorphous carbon (a-C) is given. Furthermore, some basic methods to analyze the material properties of semiconductors are described [15].

3.1 Chemical vapor deposited (CVD) diamond

Chemical vapor deposition (CVD) of diamond is currently the most popular way to produce artificial diamond. Large and thick samples of millimeter size can be fabricated [23]. Also the growth rates are reasonable, of the order of 1 $\frac{\mu m}{h}$. The quality of CVD diamond is also very good: Raman spectroscopy studies [23] show that the material consists entirely of sp^3 bonds. The major deficiency in CVD-diamond are the grain boundary defects. These defects arise from the fact that the CVD-films contain domains with different crystal orientations, thus domains with <100>, <111> and <110> orientations are all present in CVD-diamond. When these domains meet one has a grain boundary defect, which may cause defect states in the electronic gap.

The presence of oxygen and hydrogen in the CVD growth chamber plays an important role in the properties of grown films. The best diamond quality is obtained only with certain proportions of these atom species in the CVD-gas. In the diamond growth hydrogen proportion varies from 0 to 0.8 and oxygen contents from 0 to 0.6, with the requirement of the oxygen-carbon ratio being close to one. A C-H-O diagram of diamond CVD is suggested by Bachman *et al.* [24].

In the following subsections some basic techniques of CVD-diamond production are outlined.

3.1.1 CVD growth methods

A typical hot-filament CVD-reactor is depicted in Fig. 7a. In the hot filament growth a gas mixture is heated using a tungsten or tantalum filament at 2000 °C. Due to the heating, the original molecules in the CVD gas decompose into new molecular species which adsorb on the growing film.

The gas mixture consists typically of 1% methane (CH_4) and 99% H_2. The process gas breaks into various components when heated and react

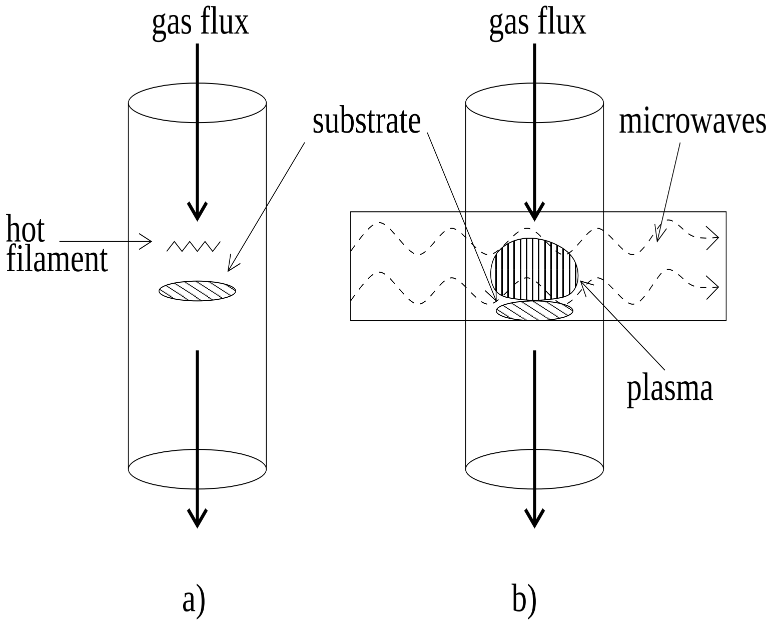

Figure 7: a) A schematic picture of a hot filament CVD reactor and b) of a microwave CVD system [15].

on the surface, thus growing a diamond film. A typical profile of the gas mixture near the growing surface is depicted in Fig. 8 [25].

The main drawback of the method is that small particles from the filament material are incorporated into the growing film.

Another CVD method is microwave CVD (Fig. 7b) [26]. The hot filament is substituted by a microwave generator. The process gas is turned into a plasma phase in a small region in space near the growing surface using the energy of the microwave field. The particles emerging from the plasma are the source of the growth. The individual reactor geometry determines the size and the shape of the plasma region. In the plasma, the molecules in the source gas are mostly decomposed into single atoms. In this method it is important to monitor the gas composition near the surface in order to keep the growth conditions constant.

3.1.2 Surface chemistry

A typical composition of the atom or molecule-flux impinging on the growing CVD-surface is shown in Fig. 8. It can be seen that on the surface the H atom, C_2H_2 (acetylene) and CH_3^- (methyl radical) are mostly present.

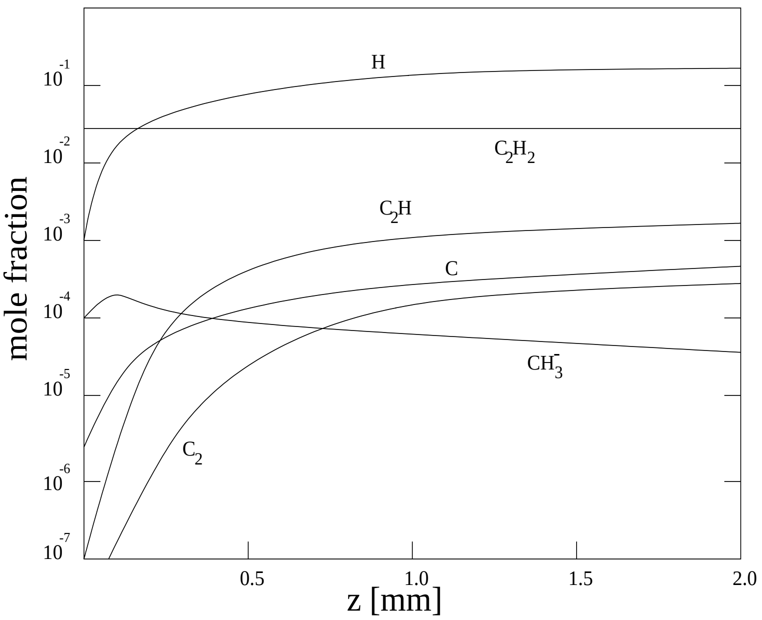

Figure 8: An example of the CVD-gas composition near the growing diamond surface (redrawn from Ref. [25]).

Especially the methyl radical is believed to constitute the key element in the CVD-growth.

The growth chemistry on the diamond $\{100\}$ surface has been most thoroughly studied by Skokov *et al.* [27]. They describe the growth process as follows. The dangling bonds of the carbon atoms on surface are mostly terminated (90 %) by hydrogen atoms. One of the H atoms of the methyl radical CH_3^- is desorbed, resulting finally in the CH_2 molecule occupying a diamond lattice position on the surface. In order to have smooth growth, the CH_2 molecules diffuse across the surface from an isolated diamond position to the end of a growing diamond-dimer chain. A schematic picture of the Skokov model is given in Fig. 9.

3.2 Amorphous carbon (a-C)

Amorphous carbon can be produced in many ways. An unfortunate general trend is that the higher the growth rate is, the less well defined is the carbon flux in particle size and in particle energy. Therefore, depending on the application, different growth methods must be chosen making a compromise between the growth rate and quality [28]. In the following sections some of

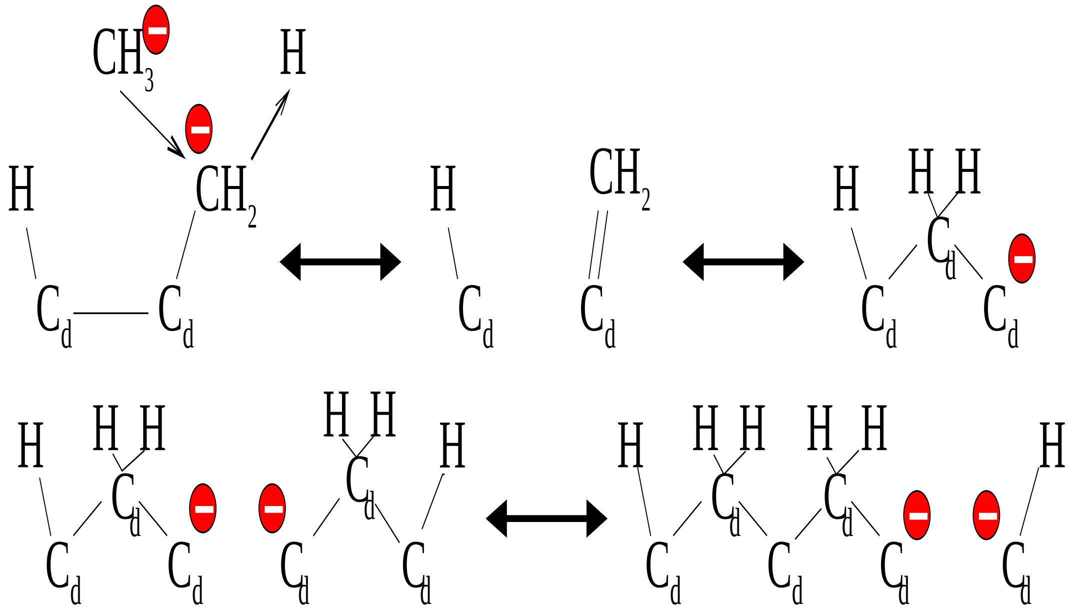

Figure 9: The Skokov-model for diamond growth has the methyl radical CH_3^- as the growth species. The five step reaction above can be described as follows. 1) The methyl CH_3^- radical absorbs at a hydrogen free dangling bond site. One of the H atoms of CH_3^- either diffuses to a neighboring dangling bond site or desorbs, leaving one unpaired electron to CH_2. 2) CH_2 makes a double bond with a surface carbon atom. Adjacent carbon-carbon bond breaks on the surface. 3) CH_2 migrates to the broken bond position and two single bonds are formed. CH_2 is now at a diamond lattice position. 4) Further CH_3^- absorb on the surface and subsequent CH_2 unit occupies diamond position. 5) CH_2 molecules migrate together growing a new dimer row on the {100} surface. Symbol C_d denotes a carbon atom at a diamond position.

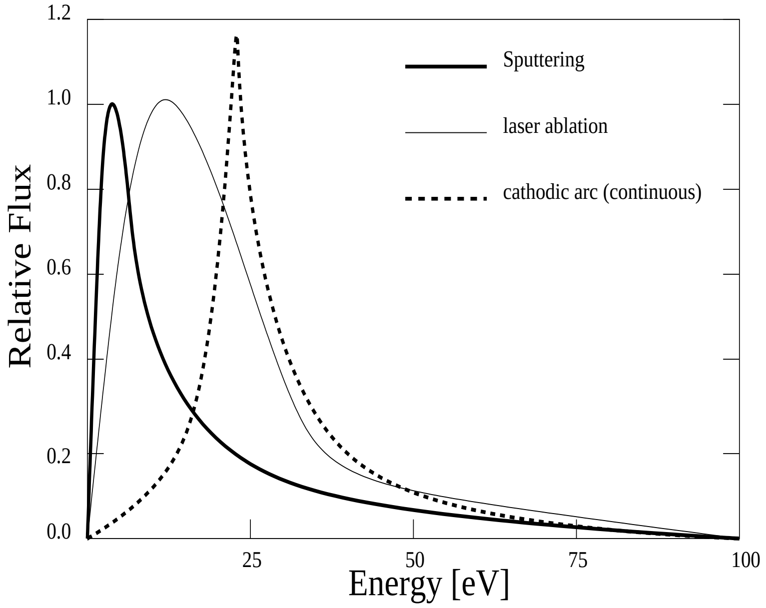

Figure 10: Different methods of producing *a-C* result to various energy distributions of the particles that impinge to the growing *a-C* surface.

the most common methods of producing *a-C* are described.

3.2.1 Cathodic arc

In the cathodic arc system a voltage pulse is applied to a graphite cathode material and a hot plasma spot is formed [29]. The physics related to the plasma is largely unknown, but at least it is known that electrons ionize carbon atoms at the cathode ($e^- + C \rightarrow 2e^- + C^+$). From the plasma spot, the majority of carbon particles (70%) emerge as singly charged C^+ ions. Magnetic lenses can be used to select ions based on the charge-mass ratio $\frac{q}{m}$ [30]. The initial energy distribution of the carbon particles without filtering is not well controlled. Typical energy distributions of the emerging particles in different growth methods of *a-C* are shown in Fig. 10.

3.2.2 Laser ablation and sputtering

A laser beam is directed at a graphite target and a flux of different carbon particles is produced from a plasma spot on the target material. The energy and size distributions are even less well defined than in the cathodic arc method, but varying the laser beam energy gives a larger range of growth energies compared to the cathodic arc deposition. A sample energy distribution is shown in Fig. 10. The laser can operate in pulse or continuous mode.

One can also produce a carbon particle flux by sputtering a graphite target with inert gas, such as Ar^+. The energy distribution of the carbon particles has a larger high-energy tail compared to the other methods (Fig. 10).

3.2.3 Mass selected ion beam epitaxy

The ion beams produced with the previously described methods (cathodic arc, laser ablation and sputtering) can be mass, charge and energy filtered. The magnetic and electric fields are utilized to separate molecules with different charge, mass and energy. Time of flight analyzers can also be applied. A severe drawback in filtering techniques is that the film growth rates are too small for commercial applications. This is due to the flatness of the distributions of mass, charge and energy with these methods [30].

3.2.4 Implantation of dopant atoms

In the CVD processes the dopant species can be mixed in the source gas. For example N_2 or B_2 have been successfully incorporated into the CVD film [31, 32].

The other possibility to incorporate the dopants into the diamond is ion implantation. In this method the energetic dopant atoms are shot into the diamond. Subsequently, the sample is annealed. Annealing means here a rapid temperature increase to recombine the interstitials and vacancies and a successive quench to stabilize the structure. In this method the kinetic energy of the dopant atom cannot be too high because permanent amorphization may result [33].

3.3 Experimental characterization of diamond-like materials

Because amorphous materials do not possess long range order, the traditional methods based on coherent diffraction, such as X-rays, cannot be applied. In the following chapters some widely utilized techniques to analyze thin diamond-like films are introduced. The most important single parameter is the sp^3 fraction in the film. Knowing it one can roughly estimate many other properties of the sample.

3.3.1 sp^3 fraction

In principle, the Extended X-ray Absorption Fine Structure (EXAFS) would be an ideal method to determine the local bonding environment of the carbon atoms. In EXAFS the information of the bonding comes from the interference pattern of a single X-ray scattering at a central-atom combined with an additional interference with the multiple scattering events of the neighbors of the central-atom, thus revealing the bonding environment of the central-atom [30]. In practice this method is still so demanding that it has not been applied to amorphous carbon on a large scale.

Electron Energy Loss Spectroscopy (EELS) is a technique to estimate the sp^2 contents in a-C. A electron beam can excite electrons from the carbon $1s$ level to $2\pi^*$. Unfortunately, transition to the σ^* state is forbidden by the electric-dipole transition selection rules. The $1s \rightarrow \pi^*$ excitation can then be seen in the energy spectra of the outcoming electron beam [30, 28]. Based on the position and magnitude of the edge of the anti-bonding (sp^2-related) π^* state the sp^2-contents can be inferred.

Nuclear Magnetic Resonance (NMR) provides an alternative way to determine the sp^3 fraction. The ^{13}C-isotope is sufficiently present (of the order of 1% [34]) in natural carbon to give a sufficient NMR signal (an ordinary ^{12}C atom has six protons and six neutrons). ^{13}C is needed because only a nucleus with an odd nuclear spin responds to the magnetic field. The chemical shifts seen by NMR caused by sp^1, sp^2 and sp^3 bonding differ and can thus be used to evaluate the proportions of the bonding types [28].

A neutron scattering experiment gives the Fourier transform of the pair-correlation function [35]. From it one can infer the average bond lengths of the material and thus estimate the sp-fractions in the films. The different bond-types are in principle clearly separated, because sp^3 has a bond length ~ 1.54 Å, $sp^2 \sim 1.41$ Å and $sp^1 \sim 1.21$ Å.

Another approach to determine the sp^3 fraction is to study the vibrational density of states of the material. The different bonding types can be identified based on the peaks in Raman spectra because they take part in different kind of lattice vibrations [36]. In Raman spectroscopy, the inelastic scattering of light is studied. Usually the energy loss in the inelastic scattering is due to phonons. The energy conservation law for scattering of a time-varying structure is

$$\hbar\omega_0 - \hbar\omega \pm \hbar\omega(\mathbf{q}) = 0, \tag{4}$$

and for momentum conservation

$$\hbar\mathbf{k}_0 - \hbar\mathbf{k} \pm \hbar\mathbf{q} + \hbar\mathbf{G} = 0. \tag{5}$$

Above $\hbar\omega_0$ and $\hbar\omega$ are the energies of incoming and outgoing light waves respectively, $\hbar\mathbf{k}_0$ and $\hbar\mathbf{k}$ their momenta. The energy and momentum of the crystal phonon excitation are $\hbar\omega(\mathbf{q})$ and $\hbar\mathbf{q}$. The extra momentum term $\hbar\mathbf{G}$ is due to the periodicity of the scattering material (*i.e.* a lattice of atoms), the $\mathbf{G}$ being any of the reciprocal lattice vectors. The term arising from a periodic lattice, $\hbar\mathbf{G}$, vanishes in amorphous structures. When the outcoming wave (energy $\hbar\omega$) acquires energy $\hbar\omega(\mathbf{q})$ one has Stokes lines, while the loss of $\hbar\omega(\mathbf{q})$ is called Anti-Stokes scattering. Not all the phonons are Raman-visible. The electromagnetic radiation (here light) couples to the lattice via the susceptibility tensor. If the susceptibility tensor has a non-vanishing derivative in the direction of the displacements belonging to the phonon in question, phonon absorption or emission can be observed [37]. Typical Raman spectra of *a-C* at various sp^3 concentrations are shown in Fig. 11. Kalish *et al.* identify the peaks in the Raman spectra as follows. The sp^2 vibrations lie at $\approx$ 1560 cm^{-1}, disorder peak at $\approx$ 1360 cm^{-1} is a finger print of nm-sized graphitic domains. The $\approx$ 960 cm^{-1} peak stems from a Si substrate and is visible only for the most transparent samples (sp^3 $\approx$ 80 %).

3.3.2 Electronic density of states

The electron density of states can be measured, for example, using photo-emission spectroscopy, electron energy loss spectroscopy (EELS) or optical absorption spectroscopy. The photo-emission spectroscopy probes the filled valence band states, EELS probes the unoccupied conduction band states while optical absorption measures the transitions between occupied and unoccupied states [39].

As described in the previous chapter, the EELS primary electron beam excites electrons to empty states. However, all transitions are not allowed because of the electric dipole transition selection rules [40]. This excitation costs energy and can be detected as energy loss of the outcoming electrons. Thus the energy difference between a known core level and the unknown level in the conduction band can be calculated [30, 28].

In photo-emission, the solid is irradiated with mono-energetic photons. The photons with energy $\hbar\omega_0$ excite electrons from occupied states to unoccupied ones. Some of the excited electrons are excited to vacuum and can

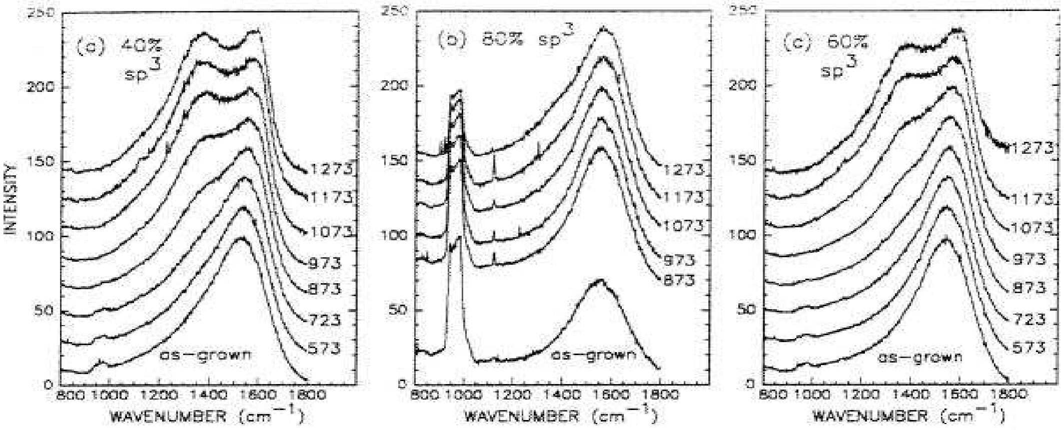

Figure 11: The visible (514 nm) Raman spectra of a) 40% b) > 80%, and c) 60% sp^3 bonded 100-nm thick *a-C* films. The figure is from Ref. [38]. The numbers in the figures after each Raman line are the corresponding temperatures of the samples.

thus be detected. The energy of the outcoming electrons is

$$E_{kin} = \hbar\omega_0 - E_i - \phi. \tag{6}$$

The E_i is the energy of the occupied electron level to be estimated. The work function ϕ of the surface should be known in order to apply this method [30].

In optical absorption electrons are excited by photons from the occupied states to the unoccupied ones. When the excitation relaxes the emitted photon gives the energy difference between the states.

The various methods of measuring the electronic structure of thin films are illustrated in Fig. 12.

3.3.3 Hardness and Young's modulus

Hardness is often measured in experiments using the so-called Vickers test. A sharp diamond tip is pushed into a surface with a given force and thereafter pulled back. The area of the depression after the Vickers hardness test is measured. Hardness is defined as the ratio between the load and the area of the depression. In the simulations another definition introduced by

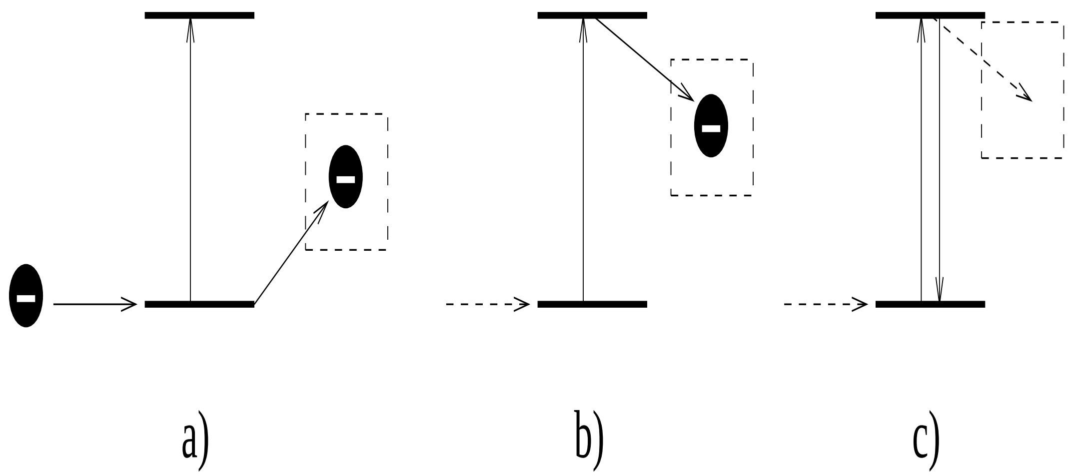

Figure 12: a) EELS: An electron loses energy in the material by means of various scattering processes. b) In photo-emission spectroscopy a photon excites an electron to vacuum. c) In optical absorption light excites an electron to an upper energy state. Dotted lines symbolize photons. The measurable observables are indicated by dashed boxes.

Pharr *et al.* is used [41]. They define hardness as

$$H = \frac{F_{max}}{A_{projected}}. \tag{7}$$

F_{max} is the maximum value of repulsive force acting on the AFM-tip measured during the loading and $A_{projected}$ is the corresponding projected contact area between the surface and the tip. In practice, the use of AFM tip for hardness measurements is not common, because the tip-surface contact area is not well known for different kinds of surfaces of macroscopical sizes.

Young's modulus, *i.e.* the stress versus strain in the film, can be approximated by employing a nano-indentation test. A sharp tip (usually diamond) is pushed into the surface, and pulled back to its original position. Young's modulus is calculated using the theory of Herzian contact

$$E^*_{sub} = \frac{\sqrt{\pi}S}{2\beta\sqrt{A}}, \tag{8}$$

where S is the unloading stiffness, *i.e.* slope of the unloading force-curve, measured at the very beginning of the unloading phase [42]. β is a coefficient depending on the tip geometry and E^*_{sub} is the reduced Young's modulus corresponding to the elastic response of both the tip and the surface [42]. The macroscopic Young's modulus E_{sub} is finally defined as

$$\frac{(1-\nu_{sub}^2)}{E_{sub}} = \frac{1}{E_{sub}^*} - \frac{(1-\nu_{tip}^2)}{E_{tip}}. \tag{9}$$

E_{tip}, ν_{tip} and ν_{sub} are the Young's modulus of the tip, the Poisson ratio of the tip and the surface, respectively. The relationship (9) assumes elastic intendation, *i.e.* that all the atomic displacements are reversible. It is based on macroscopic continuum mechanics.

4 Computational framework

In this section a brief overview of the computational methods used in this work is given. The three different levels of theory (*ab initio*, semi-classical and classical) are outlined. Additionally, methods for structural optimization and the time evolution of the system are introduced. Finally, a concept related to the electron structure calculations, **k**-point sampling, is described. A fundamental quantity in this section is the total energy of the system which is to be minimized. The minimization of the total energy is an 0 K approximation to the minimization of the free energy, which includes additionally at least vibrational and configurational entropy contributions.

4.1 Self-consistent density-functional *pseudopotential* method

In the following description two decouplings are made. Firstly, the motion of the atom nuclei is decoupled from the electrons. This is justified by the fact that the nuclei are of the order of 1000 times heavier than the electrons. Thus the electrons respond almost instantly to the movement of the atoms. This approximation is called the *Born-Oppenheimer* approximation. One can thus separately solve the electron density using Eq. (18) and move atom nuclei based on the inter-atomic forces [Eq.(17)]. Secondly, only the valence electron quasi wave functions are calculated explicitly. The core electrons are described (together with the atom nuclei) with *pseudopotentials*. In the following, the equations are given from the point of view of the *pseudopotential* approximation, *i.e.* the problem is to solve the quasi wave functions of the valence electrons. For the further reading about the density functional theory, the review articles by Payne *et al.* and by Jones *et al.* are recommended [43, 44].

Hohenberg and Kohn have shown that there is a one-to-one correspondence between the external potential (caused by the atom nuclei and core electrons) and the valence electron density [45]. Furthermore, the total energy of a given atomic configuration at the electron ground state is given as a functional of the valence electron (ve) density. The Kohn-Sham [1] total energy is written as [46]:

$$E[n_{ve}] = T^{ve-ve}[n_{ve}] + E^{ve-ve}[n_{ve}] + E^{ve-(nuc+ce)}[n_{ve}] + E^{xc}[n_{ve}] + E^{nuc-nuc}. \tag{10}$$

[1] The elementary charge e is a positive number throughout this work, its value is 1.60 $\times 10^{-19}$ coulomb.

Here the valence electron density n_{ve} is defined (with the spin degeneracy) as

$$n_{ve}(\mathbf{r}) = 2\sum_{i\in ve} \psi_i \psi_i^*. \tag{11}$$

The kinetic energy of the non-interacting valence electrons is defined (with the spin degeneracy) as

$$T^{ve-ve}[n_{ve}] = 2\sum_{i\in ve} \int \psi_i \frac{\hbar^2}{2m} \nabla^2 \psi_i^* d^3r, \tag{12}$$

and valence electron- valence electron interaction as:

$$E^{ve-ve}[n_{ve}] = \frac{e^2}{2} \int \frac{n_{ve}(\mathbf{r}) n_{ve}(\mathbf{r}')}{|\mathbf{r}-\mathbf{r}'|} d^3r\ d^3r'. \tag{13}$$

The energy of the interactions between the valence electrons and the nucleus together with the core electrons is calculated from

$$E^{ve-(nuc+ce)}[n_{ve}] = \int V^{nuc+ce}(\mathbf{r}) n_{ve}(\mathbf{r}) d^3r. \tag{14}$$

Above V^{nuc+ce} is the potential due to the nucleus (nuc) and the core electrons (ce). It will be discussed later in this section.

$E^{xc}[n_{ve}]$ is the exchange-correlation energy of the valence electrons with the exchange-correlation energy density ϵ^{xc} of a homogeneous electron gas of the same density

$$E^{xc}[n_{ve}] = \int \epsilon^{xc}_{hom}[n_{ve}(\mathbf{r})] n_{ve}(\mathbf{r}) d^3r. \tag{15}$$

Above $\epsilon^{xc}_{hom}[n_{ve}(\mathbf{r})]$ is the exchange-correlation energy density of a homogeneous electron gas with the given density $n_{ve}(\mathbf{r})$. It can be calculated accurately [47]. The LDA approximation treats the exchange-correlation part of the energy as a sum of exchange-correlation energies of small volumes of homogeneous electron gas. The physical meaning of the exchange energy is the energy obtained due to the Pauli principle: the electrons with the same spin cannot occupy the same region in space. This requirement decreases the Coulomb energy of the system (because the Pauli principle keeps electrons with the same spin apart from each other). This energy is taken into account in the well-known Hartree-Fock approximation [47, 48].

The correlation energy is the energy gained when additionally separating the mutually repelling electrons with different spins. The pay off in this case is an increase in the kinetic energy of the system, because keeping the two electrons apart enhances the curvature of the wave functions and thus the kinetic energy term T[n_{ve}] in Eq. (10) increases.

Finally the repulsive energy between the nuclei is described as:

$$E_{nuc-nuc} = \frac{1}{2}\sum_{I\neq J}\frac{Z_I Z_J e^2}{|\mathbf{R_I} - \mathbf{R_J}|}. \tag{16}$$

This term is calculated in practice using the Ewald summation technique, because the real-space summation converges poorly [49]. Additionally, the reciprocal space the Ewald summation adds up the divergent parts of the electron-electron and electron-ion energies [$E^{ve-ve}[n_{ve}]$ and $E^{ve-(nuc+ce)}[n_{ve}]$ in Eq. (10)] in such a way that the divergences cancel.

The force acting on the atom j, in direction p, is obtained by taking the negative derivative

$$F_{j,p} = -\frac{\partial E}{\partial R_{j,p}}. \tag{17}$$

It is important to notice that every term in Eq. (10) is dependent on the atomic positions $\mathbf{R_j}$

It remains to solve the Kohn-Sham one electron valence electron wave functions. This is done by minimizing the total energy [Eq. (10)] with respect to ψ_i^*. One arrives at the Kohn-Sham equations

$$\left(\frac{-\hbar^2}{2m}\nabla^2 + V^{nuc+ce}(\mathbf{r}) + e^2\int\frac{n_{ve}(\mathbf{r'})}{|\mathbf{r}-\mathbf{r'}|}d^3\mathbf{r'} + \frac{\partial(n_{ve}(\mathbf{r})\epsilon_{hom}^{xc}[n_{ve}(\mathbf{r})])}{\partial n_{ve}(\mathbf{r})}\right)\psi_i(\mathbf{r}) = \epsilon_i\psi_i(\mathbf{r}). \tag{18}$$

The Kohn-Sham equations describe non-interacting electrons moving in the potential caused by the other electrons [43]. In the *pseudopotential* approximation (to be described below) only the wave functions of the valence electrons (ve) are explicitly taken into account. The first term in the Kohn-Sham Hamiltonian is the kinetic energy operator, the second the potential of atom nuclei and core electrons (ce), the third the potential due to other valence electrons , and the fourth the exchange and correlation potential of the valence electrons. In order to find the lowest energy electron configuration, the Kohn-Sham equations are solved self-consistently so that the change in the sum of the electron energy-levels (or in the electron density) is less than a given tolerance. At the ground state (the lowest energy state of the system) the Kohn-Sham-iterated electron wave functions give the correct ground state energy [Eq. (10)] [46, 45]. On the contrary, the summation of the energies of the occupied electron states ϵ_i in Eq. (18) does not give the correct total energy because of the over counting the electron-electron and exchange-correlation terms. To gain the total energy of the ground state, the Kohn-Sham energy functional (without spin) is used [Eq. (10)]. The wave functions are now the ones calculated self-consistently from Eq. (18).

The potential due to the nucleus and the core electrons acting on the valence electrons $V^{nuc+ce}(\mathbf{r})$ is approximated with a *pseudopotential*. The idea of the *pseudopotential* is to mimic the true all-electron potential in the space region where the inter-atomic bonds are located and to give an approximation of the true potential near the atom nuclei. The gain is in the computing time: if the charge of the nuclei and core electrons can be approximated with a smooth function, the number of plane-waves [Eq. (49)] is reduced drastically. The core electrons do not contribute much to the bonding of the system and thus in order to obtain correct geometries and valence electron densities it is enough to describe the potential correctly outside the core region and approximately in the core region. To accomplish this the all-electron wave function is solved for a single atom using a scalar-relativistic Schrödinger equation [50, 51]. A spherically symmetric electron configuration for the single atom is chosen, so that the solutions of the relativistic Schrödinger equation are characterized by the angular momentum quantum number l. The pseudo valence wave functions are obtained by requiring the identity of the logarithmic derivative of the all-electron valence wave functions and the pseudo valence wave functions beyond a given core radius. The core radius is usually chosen in the middle of the outermost node and the outermost extremum of the all-electron wave function with quantum number l. Moreover, the true all-electron wave functions and pseudo valence wave functions should correspond to the same eigenvalue. Screened *pseudopotentials* are solved from the inverted scalar-relativistic Schrödinger equation using the calculated all-electron energy levels. The final unscreened *pseudopotentials* are then constructed by subtracting the electron-electron and the exchange-correlation potential of the all-electron charge from the screened *pseudopotential*. The unscreened *pseudopotential* $V^{nuc+ce}(\mathbf{r})$ can then be used in Eqs. (18) and (10) to describe the interaction between valence electrons and nuclei plus core electrons.

4.2 Density-functional based tight-binding method (DFTB)

An excellent review article by Goringe *et al.* summarizes the general theoretical basis of the tight–binding method and the current progress in the theory [52].

The DFTB-methodology in particular has been described in detail in references [53, 54]. The background idea within this scheme is the expansion of the molecular wave function Ψ in a basis set of atom centred (localized) orbitals ϕ_ν. Such a method is widely known as a linear combination of atomic orbitals (LCAO).

The atomic orbitals are represented by Slater-type radial functions separated from the spherical harmonics $Y_{l,m}$.

$$\phi_\nu(\mathbf{r}) = \phi_{n,l,m}(\mathbf{r}) = \sum_{i=1}^{N_i}\sum_{j=1}^{N_j} a_{n,i,j} r^{l+i-1} e^{-\alpha_j r} Y_{l,m}(\frac{\mathbf{r}}{r}). \tag{19}$$

Here, $\mathbf{r}$ is the position vector of an electron, while the main n and the angular momentum quantum numbers l, m have been combined to the superindex ν. The exponential factors α_j ($N_j \approx 5$) are chosen to yield an accurate basis set [53], while N_i is typically about 4.

The set of coefficients $a_{n,i,j}$ for each atom type can then be obtained by solving the set of Kohn-Sham equations for single atoms. The key difference of the DFTB compared to the other LCAO-schemes is, however, that in the DFTB approach the single-atom Schrödinger equation is modified by an artificial potential which essentially redistributes the electron density far apart from the nucleus of the single atom and maintains the wave function near the atom [53]. This is usually referred to as contraction or confinement potential for the wave function. The "confined" Kohn-Sham equation is defined as follows:

$$\left(\frac{-\hbar^2}{2m_e}\nabla^2 + V^{nuc+ce} + e^2\int \frac{n_{ve}(\mathbf{r}')}{|\mathbf{r}-\mathbf{r}'|}d^3\mathbf{r}' + \frac{\partial(n_{ve}(\mathbf{r})\epsilon^{xc}_{hom}[n_{ve}(\mathbf{r})])}{\partial n_{ve}(\mathbf{r})} + (\frac{r}{r_0})^2\right)\phi_\nu(\mathbf{r}) = \epsilon_\nu\phi_\nu(\mathbf{r}). \tag{20}$$

The last term is the confinement potential causing the atom centred orbitals ϕ_ν to set up a more appropriate molecular wave function in interatomic regions of a given multi-atom structure, while not disturbing the wave function closer to atoms too much. In this sense the modified (pseudo-) atomic orbitals are constructed as to predict a "bulk-like" behavior. The meaning of the various other terms is the same as in usual Kohn-Sham theory (which is explained in detail after Eq. (18) in the previous chapter).

The single atom equations are solved within density functional theory using the local density or generalized gradient corrected local density approximations for the exchange-correlation potential (as described in the previous chapter). The self-consistent solution yields the basis set functions ϕ_ν for the valence electrons making use of a *pseudopotential* approach which describes the core electrons approximately (see the previous chapter).

Given this basis set the Kohn-Sham-equations of the many-body system(*i.e.* many-atom and many-electron) can be transformed into algebraic secular equations for the expansion coefficients of the many-body wave function $\Psi(\mathbf{r})$ [Eq. (25)]. The Hamiltonian matrix elements entering the secular equations are obtained by replacing the effective potential V_{eff} of the many-body system by a simple superposition of neutral atom centred potentials.

$$V_{eff}(\mathbf{r}) = \sum_m V_0^m(|\mathbf{r} - \mathbf{R}_m|). \tag{21}$$

Here, $\mathbf{R_m}$ is the position vector of the m'th atom. The neutral potentials V_0^m are constructed from the confined atomic wave functions or densities and are of the form

$$V_0^m(r) = V^{nuc+ce} + e^2 \int \frac{n^m_{ve-comp}(\mathbf{r}')}{|\mathbf{r} - \mathbf{r}'|} d^3\mathbf{r}' + \frac{\partial(n^m_{ve-comp}(\mathbf{r})\epsilon^{xc}_{hom}[n^m_{ve-comp}(\mathbf{r})])}{\partial n^m_{ve-comp}(\mathbf{r})}. \tag{22}$$

Note that no further confinement is applied at this point.

The molecular orbitals for the many-body system are obtained by a linear combination of the confined atom-centred wave functions as discussed above

$$\psi_i(\mathbf{r}) = \sum_{\nu,m} C^i_\nu \phi_\nu(\mathbf{r} - \mathbf{R}_m). \tag{23}$$

One can also include the periodic boundary condition to the DFTB-formalism by requiring that the wave function is of Bloch-type *i.e.* that the atom-centred wave is multiplied by a lattice periodic plane wave,

$$\psi_{i,\mathbf{k}}(\mathbf{r}) = \sum_{\nu,m} C_{\nu,i} e^{i\mathbf{k}\cdot\mathbf{R_m}} \phi_\nu(\mathbf{r} - \mathbf{R}_m). \tag{24}$$

Using these expressions the secular equations become in matrix notation

$$\sum_{\nu} C_{\nu,i}(h_{\mu,\nu} - \epsilon_i s_{\mu,\nu}) = 0, \forall \mu, i \tag{25}$$

where the Hamiltonian and overlap matrix elements contain either the real-space elements or the Fourier transformed **k**-dependent reciprocal-space elements.

Given the confined wave functions ϕ_ν and the neutral atom-centred potentials V_0^m the real-space Hamiltonian matrix elements can be calculated (at the Γ point):

$$h_{\mu,\nu} = \begin{cases} < \phi_\mu | -\frac{\hbar^2}{2m_e}\nabla^2 + V_0^m + V_0^n | \phi_\nu > & \text{if } \mu \in m \text{ and } \nu \in n \\ \epsilon_{freeatom} & m = n, \mu = \nu \\ 0 & m = n, \mu \neq \nu. \end{cases} \qquad s_{\mu,\nu} = < \phi_\mu | \phi_\nu > \tag{26}$$

The indices m and n again refer to atoms while μ,ν denote the set of quantum numbers (n, l, m) characterizing the localized atomic orbitals. The approximation made at this point is known as the two-centre evaluation, as integrals involving more than two wave functions are neglected. In this way the amount of computational effort to calculate the integrals in Eq. (26) is enormously reduced. This approximation is connected with the confinement of orbitals which due to the reduction of orbital overlap in regions far apart from atom-centres causes higher centre integrals to be relatively small compared to two-centre contributions. DFTB further takes advantage of the fact that these two-centre integrals may be tabulated as a function of distance between two pseudo-atomic orbitals. Such integrals calculated for a standard orientation of orbitals can then easily be transformed into the true contributions in a many-body system by the rules first published by Slater and Koster [55]. Under these circumstances the generation of the pseudo-atomic orbitals and the numerical evaluation of Hamiltonian and overlap matrix elements for any combination of two such orbitals can be done prior to the many-atom calculation in a separate manner. In the actual many-atom calculation, the tabulated values are read by the DFTB-programs, rotated and interpolated for the geometries in question.

A further approximation is the non-self-consistent solution of the coefficients $C_{\nu,i}$ in Eq. (25). The values for the coefficients of the wave functions are solved only once for each atomic configuration. In self-consistent calculations the $C_{\nu,i}$ are iterated until they change less than a given tolerance. Recently, a charge self-consistent version of the DFTB-code has been written and demonstrated [56]. The charge self-consistency increases the computational cost by a factor of 3-5. It is necessary for systems with large charge transfers, such as for polar surfaces.

Finally the total energy within the DFTB may be written as

$$E_{tot} = \sum_i \int \epsilon_{i,\mathbf{k}} \, d\mathbf{k} + E_{rep}, \tag{27}$$

where E_{rep} is an energy term which represents overcounting corrections of the Hartree and exchange-correlation energies plus the ion-ion core repulsion. As in other tight-binding methods, this part of the total energy is modeled by a classical potential which is obtained as a function of distance between atom-centres by calculating self-consistent field DFT energies, E_{DFT}, for given reference systems and setting $E_{rep} = E_{DFT} - \sum_i \int \epsilon_{i,\mathbf{k}} \, d\mathbf{k}$.

The forces acting on atoms are obtained in a similar way as in the DFT case (previous chapter), *i.e.* by taking derivatives of the total energy with respect to the atom positions.

4.3 Empirical (*i.e.* classical) Tersoff potential

The empirical Tersoff potential has given good results in modeling amorphous carbon and diamond [60]. Also other empirical potentials have been used to simulate *a-C* and diamond [58, 59]. The motivation of the form of the Tersoff potential in Eqs. (28) - (30) is twofold. Firstly, the energy per bond decreases with increasing number of bonds of an atom. Secondly, the presence of a bond weakens other bonds, this weakening increasing when the two bonds come near to each other. Based on these arguments Tersoff formulates his potential as follows [57].

$$\begin{aligned} E_{tot} &= \frac{1}{2} \sum_{i \neq j} V_{ij}, \\ V_{ij} &= f_C(r_{ij}) b_{ij} f_A(r_{ij}). \end{aligned} \tag{28}$$

The f_R represents a repulsive pair potential, f_A is the attractive part and function f_C provides a smooth cut-off. The b_{ij} contains the bond angle dependent terms and a_{ij} limits the range in distance for the angle dependent b_{ij}. Indexes i, j, and k in the equations refer to atoms. The form of the terms in the pair potential are:

$$
\begin{aligned}
f_R(r_{ij}) &= A\exp\Big(-\lambda_1 r_{ij}\Big),\\
f_A(r_{ij}) &= -B\exp\Big(-\lambda_2 r_{ij}\Big),\\
f_C(r_{ij}) &= \begin{cases} 1 & r_{ij} < R-D,\\ \frac{1}{2}-\frac{1}{2}\sin\left(\frac{\pi}{2D}(r-R)\right) & R-D < r_{ij} < R+D,\\ 0 & r_{ij} > R+D. \end{cases}
\end{aligned}
\tag{29}
$$

Thus the potential vanishes smoothly when the distance increases from R to D. The angle dependent part is taken as

$$
\begin{aligned}
b_{ij} &= (1+\beta^n\phi_{ij}^n)^{-1/2n},\\
\phi_{ij} &= \sum_{k\neq i,j} f_C(r_{ik})g(\theta_{ijk})\exp\Big(\lambda_3^3(r_{ij}-r_{ik})^3\Big),\\
g(\theta) &= 1+\frac{c^2}{d^2}-\frac{c^2}{d^2+(h-\cos\theta)^2}.
\end{aligned}
\tag{30}
$$

Where the θ_{ijk} is the angle between bonds ij and ik. The numerical parameters for carbon can be found in Ref. [60]. The main deficiency of the Tersoff potential is a poor description of π bonding between sp^2 bonded atoms. The parameters in the potential are fitted so that the cohesive energies of diamond and graphite are reproduced. Additionally, the fit is made for the bulk modulus and the lattice constant of diamond.

4.4 Algorithms for moving atoms

In this subsection some of the methods to carry out direct energy minimization, diffusion at zero temperature and molecular dynamics (MD) simulation are introduced.

4.4.1 Conjugate gradient (CG) energy minimization

We limit the description of the CG method in the case when the function E (typically the total energy of system) to be minimized is estimated by the

Taylor series of the second order *i.e.*

$$E(\mathbf{x}) = E(\mathbf{P}) + \sum_i \frac{\partial E}{\partial x_i} x_i + \frac{1}{2}\sum_{i,j} \frac{\partial^2 E}{\partial x_i \partial x_j} x_i x_j + \cdots \approx c - \mathbf{b}\cdot\mathbf{x} + \frac{1}{2}\mathbf{x}\cdot\mathbf{A}\cdot\mathbf{x}, \tag{31}$$

where $c \equiv E(\mathbf{P}), \mathbf{b} \equiv -\nabla E|_{\mathbf{P}}$, $[\mathbf{A}]_{ij} \equiv \frac{\partial^2 E}{\partial x_i \partial x_j}|_{\mathbf{P}}$, and $\mathbf{P}$ is the centre of the Taylor expansion. Solving the gradient from Eq. (31), yields

$$\nabla E = \mathbf{A}\cdot\mathbf{x} - \mathbf{b}. \tag{32}$$

In the steepest descent method one moves particles according to forces $-\nabla E$ which usually leads to poor convergence. This is because the minimization in one direction spoils partly the minimization to the other directions. In order to avoid this problem, the CG approach starts from the requirement that energy minimization in one direction does not destroy the minimization in any other direction. Consider a change in the gradient when moving to some direction $\delta\mathbf{x}$

$$\delta(\nabla E) = \mathbf{A}\cdot\delta\mathbf{x}. \tag{33}$$

Suppose that one has at the previous minimization step moved along $\mathbf{u}$ and minimized the function E in that direction. Then the requirement that the next minimization direction $\mathbf{v}$ does not spoil the minimization along $\mathbf{u}$ is that the change in the gradient $\delta\nabla E$ is perpendicular to $\mathbf{u}$. By Eq. (33) this means

$$0 = \mathbf{u}\cdot\delta(\nabla E) = \mathbf{u}\cdot\mathbf{A}\cdot\mathbf{v}. \tag{34}$$

Supposing that one has the sequence conjugated search directions $\mathbf{h_i}$, *i.e.* $\mathbf{h_i}\cdot\mathbf{A}\cdot\mathbf{h_{i+1}} = 0$, it is enough to minimize the function E subsequently along these directions $\mathbf{h_i}$ in order to arrive at a (local) minimum of the function E. This does not require any knowledge of the Hessian matrix $\mathbf{A}$. The next point in space, $\mathbf{x_{i+1}}$, is selected by choosing the coefficient λ_i in such a way that the function has a minimum in the search direction $\mathbf{h_i}$ *i.e.*

$$\mathbf{x_{i+1}} = \mathbf{x_i} + \lambda_i\mathbf{h_i}. \tag{35}$$

The subsequent minimization directions are generated by the following formulas

$$\mathbf{h_{i+1}} = -\nabla E(\mathbf{x_{i+1}}) + \alpha_i\mathbf{h_i} \tag{36}$$

at point $\mathbf{x_{i+1}}$. The unknown coefficient α_i is derived in Ref. [61] to have a value

$$\alpha_i = \frac{[-\nabla E(\mathbf{x_{i+1}}) + \nabla E(\mathbf{x_i})] \cdot -\nabla E(\mathbf{x_{i+1}})}{\nabla E(\mathbf{x_i}) \cdot \nabla E(\mathbf{x_i})}. \tag{37}$$

The conjugate gradient method finds the energy minimum in maximally N steps, where N is the dimension of the space (usually three times the number of atoms). This convergence requires that the function can be roughly approximated by Eq. (31).

4.4.2 Finding diffusion barriers by the projected conjugate gradient (PCG) method

To find relevant diffusion barriers along diffusion paths, we utilize a method recently introduced to specify changes in barrier heights on top of diamond surfaces due to the presence of dopants in subsurface layers (see Publication 4). In this particular scheme single energy barriers are found by a series of conjugate gradient (CG) relaxation processes with modified forces for the diffusing atom. The principle is similar to what has been introduced in the activation-relaxation technique [62, 63]. In our method, however, the force on the diffusing atom is projected onto equidistant planes which are always perpendicular to the global search direction . Therefore, the diffusing atom can only relax within these virtual planes, whereas all other atoms can fully relax due to the true interatomic forces acting on them.

Between two consecutive CG steps the diffusing atom is pushed from the current to the next plane on a straight line connecting the position in the current plane with the final point on the global search direction. Then the whole system is CG relaxed under the restrictions described above.

Note that all atoms can react to the changes in the position of a single mover and that the particles can even get around huge barriers that may exist along the global search direction. Fig. 13 shows a snapshot of a typical situation when searching for a single barrier. The solid circles indicate the initial and final position of the moving atom, dotted circles mark its positions along the migration path at various steps of the calculation. The start and end points along the global search direction which is marked by the straight dashed line for the i^{th} single mover are indicated by $\mathbf{r}^i_{initial}, \mathbf{r}^i_{final}$ respectively. The relaxed position of the mover in one of the planes is $\mathbf{r}^i_{current}$.

As discussed above, in any diffusion step the mover is initially set to the crossing point of the next plane along the global search path and the vector

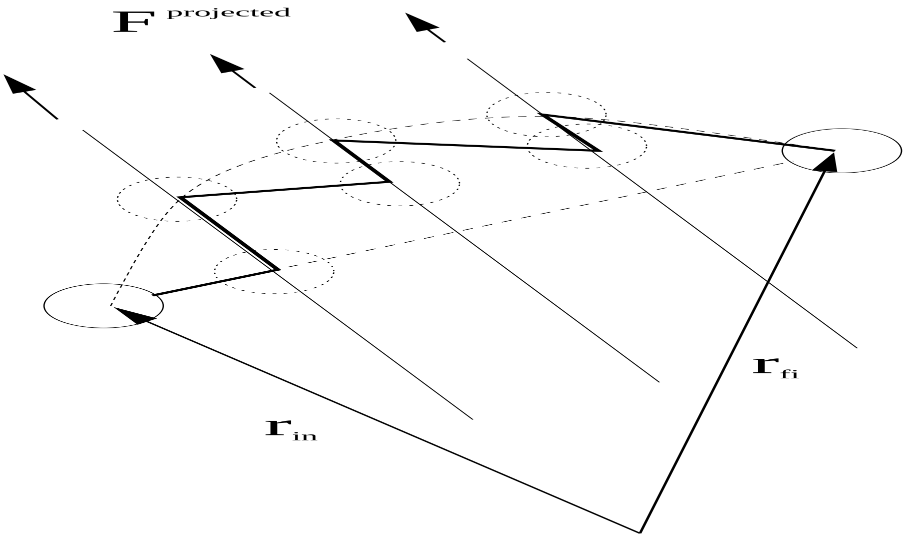

Figure 13: The projected conjugate gradient method. Here the diffusing atom is moved in four steps from the initial position r_{in} to the final position r_{fi}. Forces $F_{projected}$ acting on the diffusing atom are restricted to the planes perpendicular to the diffusion direction during the CG minimization.

$\mathbf{r}^i_{final} - \mathbf{r}^i_{current}$. Therefore, the mover will be always focused back onto the global search direction so that the search path cannot diverge which is the major difficulty in another study [64] that attempts to find all the local barriers. The position of atom i in the next virtual plane is given by

$$\mathbf{r}^i_{next} = \mathbf{r}^i_{current} + \frac{\mathbf{r}^i_{final} - \mathbf{r}^i_{current}}{n_{total} - n_{current}}, \tag{38}$$

where n_{total} is the total number of steps between the initial and the final point along the global search direction. This is the parameter which determines the accuracy of the barrier height finally found. It is chosen such that the step length (*i.e.* the distance between the adjacent planes in Fig. 13) $\frac{\mathbf{r}^i_{final} - \mathbf{r}^i_{initial}}{n_{total}}$ becomes so small that the desired accuracy in the height of the energy barrier can be obtained.

There is a certain degree of freedom how to pick the final position of a mover along a selected global search direction. In order to make the algorithm very much independent of this choice the position is set quite far away (> 100 Å) from the initial local minimum. This is possible since the search for saddle points in the vicinity of the global search direction is terminated as soon as the first relevant saddle is found. The maximum number of search steps determines the distance between the virtual planes that restrict the motion of the mover. For example one can use $\mathbf{r}^i_{final} - \mathbf{r}^i_{initial}$ = 100 Å, n_{total} = 2000 yielding a spacing of 0.05 Å.

The number of search steps already made ($n_{current}$) ranges from zero to $n_{total} - 1$. The single search step is finished by relaxing the system with the CG method allowing all atoms in the structure to change their positions while constraining the mover onto the plane perpendicular to $\mathbf{r}^{initial} - \mathbf{r}^{final}$. The projected force for such a diffusing atom is calculated as

$$F^p_{projected} = F^p - (r^p_{final} - r^p_{initial}) \cdot \frac{(\mathbf{F} \cdot \Delta\mathbf{r})}{|\Delta\mathbf{r}|^2}, \tag{39}$$

where $\Delta\mathbf{r} = \mathbf{r}_{final} - \mathbf{r}_{initial}$, and p denotes the x, y or z coordinates. The projected force is substituted for the true total force acting on the diffusing atom. After this procedure the CG total energy minimization operates in the usual way. Note also that projecting forces before actually calling the CG algorithm is sufficient for all of the subsequent CG steps since the conjugated directions constructed during the minimization of the energy functional depend linearly on the initial data.

4.4.3 Molecular dynamics (MD) simulations with a thermal coupling

Usually, at the beginning of a molecular dynamics simulation run, random velocities drawn from the *Maxwell-Bolzmann* distribution corresponding to a desired temperature are given to atoms. Thereafter the system is allowed evolve according to the Newton's equations of motions, possibly applying a thermal coupling algorithm in order to keep the system at the desired temperature. The Newton's equations of motions are integrated in time using the Verlet algorithm. The atom position $\mathbf{r}$ is expanded at time t = t_0 + Δt using a Taylor series

$$\mathbf{r}(t_0 + \Delta t) = \mathbf{r}(t_0) + \mathbf{v}(t_0)\Delta t + \frac{\mathbf{f(t_0)}}{2m}\Delta t^2 + \frac{\dddot{\mathbf{r}}}{3!}\Delta t^3 + \mathcal{O}((\Delta t)^4), \tag{40}$$

and at time = t_0 - Δt

$$\mathbf{r}(t_0 - \Delta t) = \mathbf{r}(t_0) - \mathbf{v}(t_0)\Delta t + \frac{\mathbf{f(t_0)}}{2m}\Delta t^2 - \frac{\dddot{\mathbf{r}}}{3!}\Delta t^3 + \mathcal{O}((\Delta t)^4), \tag{41}$$

$\mathbf{f}$ denoting the force acting on the atom in question. Adding up these two equations gives

$$\mathbf{r}(t_0 + \Delta t) + \mathbf{r}(t_0 - \Delta t) = 2\mathbf{r}(t_0) + \frac{\mathbf{f(t_0)}}{m}\Delta t^2 + \mathcal{O}((\Delta t)^4), \tag{42}$$

or

$$\mathbf{r}(t_0 + \Delta t) \approx 2\mathbf{r}(t_0) - \mathbf{r}(t_0 - \Delta t) + \frac{\mathbf{f(t_0)}}{m}\Delta t^2, \tag{43}$$

which is the formula most commonly used in MD simulations. The velocities $\mathbf{v}(\mathrm{t})$ can be solved using

$$\mathbf{r}(t + \Delta t) - \mathbf{r}(t - \Delta t) = 2\mathbf{v}(t) + \mathcal{O}((\Delta t)^3), \tag{44}$$

which requires the storage of the atomic positions for at least three time steps [65].

In this work two kinds of thermostats have been utilized in order to keep the system at constant temperature. Firstly, the Berendsen method has been applied [66]. It has the purpose to make the temperature T decay slowly to an external reference temperature T_0 with a time constant τ_T for the coupling

$$\frac{dT}{dt} = \frac{T - T_0}{\tau_T}. \tag{45}$$

This can be accomplished by adding a kind of friction term to the equations of motion

$$\dot{v}_i^p = \frac{f_i^p}{m} - (\frac{T_0}{T} - 1)\frac{v_i^p}{2\tau_T}, \tag{46}$$

where the index i refers to atom index and p denotes the x, y or z directions. This leads in practice to the scaling of the velocities by a factor λ

$$\lambda = \sqrt{1 + (\frac{\Delta t}{\tau_T}(\frac{T_0}{T} - 1)}, \tag{47}$$

where the Δt is the time step used in the MD simulation.

Secondly, the direct velocity scaling has been used. This means that the atomic velocities are rescaled after a certain number (typically 10) MD-steps using a rescaling factor, which is greater then one if the instant temperature is below the desired value and less than one in the opposite case. Simultaneously the total impulse of the system is required to be zero.

4.5 k-point sampling

The effect of periodicity of the system must be taken into account in electron structure calculations, such as described in sections 4.1 and 4.2. In the following a brief introduction to the **k**-point sampling is given. The concept of **k**-point sampling is usually connected with the so called super-cell approximation. In a super-cell calculation an atomic-size piece of material is built: a super-cell. This super-cell is repeated in all three dimensions in order to fill the space. Usually a super-cell consist of a defect surrounded by atoms at ideal lattice sites. If one neglects the periodicity in a super-cell calculation one talks about the Γ-point approximation. It may be justified, for example, when studying point defects in the limit of a large super-cell.

The band index k is left out in Eqs. (12)- (16) and in the calculation of the valence electron density n_{ve}. In the periodic systems the physical quantities Q are obtained by averaging over **k**-points with weights w_k

$$Q = \sum_k w_k q_k. \tag{48}$$

For a review of the **k**-point sampling in periodic systems see the articles by Froyen *et al.* and Monkhorst & Pack [67, 68]. There the calculation of the weight factors w_k for different Bravais lattices are carried out. For the definitions of Bravais lattices and related topics see [37, 47].

The most commonly used basis set in electron structure calculations nowadays is the set of plane waves. Thus the wave functions are described as (summation over **G** vectors):

$$\psi_{j,k}(\mathbf{r}) = e^{i\mathbf{k}\cdot\mathbf{r}} \sum_{\mathbf{G},\frac{1}{2}|\mathbf{G}+\mathbf{k}|\leq E_{cut}} c_{j,\mathbf{G}+\mathbf{k}} e^{i\mathbf{G}\cdot\mathbf{r}} = e^{i\mathbf{k}\cdot\mathbf{r}} u_k(\mathbf{r}). \tag{49}$$

Above, $u_k(\mathbf{r}) = u_k(\mathbf{r}+\mathbf{r_n})$, is a function with a lattice periodicity, such as for example an atom-centred orbital. The unknown coefficients $c_{j,\mathbf{G}+\mathbf{k}}$ are solved when solving the Kohn-Sham equations [Eq. (18)], as described in Sec. 4.1. The allowed values for the **G** vectors are governed by the periodicity of the Bravais lattice:

$$\mathbf{G} = n_1\mathbf{b_1} + n_2\mathbf{b_2} + n_3\mathbf{b_3}, \qquad n_1, n_2, n_3 \in \mathbb{Z}. \tag{50}$$

The summation is carried out up to a given cut-off energy E_{cut}. The Bloch condition for the wave function

$$\psi_{j,k}(\mathbf{r}+\mathbf{R}) = e^{i\mathbf{k}\cdot\mathbf{R}} \psi_{j,k}(\mathbf{r}) \tag{51}$$

and the boundary condition due to the finite size of the physical object

$$\psi_{j,k}(\mathbf{r} + N_p\mathbf{a_p}) = \psi_{j,k}(\mathbf{r}) \tag{52}$$

yield together a condition for the allowed $\mathbf{k}$ values in the direction p (p labeling the Bravais lattice vectors $\mathbf{a_1}$, $\mathbf{a_2}$ and $\mathbf{a_3}$)

$$\mathbf{k_p} = \frac{m}{N_p}\mathbf{b_p}, \quad m \ integer. \tag{53}$$

Above, the vector $\mathbf{R}$ is any of the vectors in the Bravais lattice. $N_p\mathbf{a_p}$ is the dimension of the physical object in the direction $\mathbf{a_p}$ and $\mathbf{b_p}$ is the primitive reciprocal lattice vector corresponding to the real-space Bravais lattice vector $\mathbf{a_p}$ [37]. However, in the calculations, instead of a physical object one has a small volume of atoms, the so called super-cell. This volume is repeated infinitely in all three Bravais lattice directions to fill all the space. Thus N_p in Eq. (53) approaches infinity, and $\mathbf{k_p}$ in Eq. (53) can be regarded as a continuous variable. This means that all $\mathbf{k}$-points are allowed in the supercell calculations and they lie infinitely dense. Because of the periodicity of the wave function $\psi_{j,\mathbf{k}_{arb}} = \psi_{j,\mathbf{k}_{1BZ}+\mathbf{G}} = \psi_{j,\mathbf{k}_{1BZ}}$ and a physical quantity Q ($\mathbf{k}_{arb}$) = Q ($\mathbf{k}_{1BZ}$ + $\mathbf{G}$) = Q ($\mathbf{k}_{1BZ}$) the sampling of the infinite set of allowed $\mathbf{k}$ values can be restricted to the first Brillouin zone (BZ). Furthermore, because of the physical quantities vary slowly with $\mathbf{k}$, one can sample the continuum of the $\mathbf{k}$-values with a set of discrete $\mathbf{k}$-points. Above an arbitrary $\mathbf{k}$-point $\mathbf{k}_{arb}$ is transferred into the first BZ with $\mathbf{k}_{arb} = \mathbf{k}_{1BZ} + \mathbf{G}$, where $\mathbf{k}_{1BZ}$ belongs to the first BZ, and the $\mathbf{G}$-vector belongs to the reciprocal lattice.

Finally, let us consider a practical point in the calculations, namely the equivalent sampling of $\mathbf{k}_{1BZ}$-points when changing the size of the super-cell. This procedure is used when one wants to know when the size of the super-cell is big enough so the point defects in the neighboring super-cells do not interact with each other. The convergence is reached when the increase in the size of the super-cell with an equivalent $\mathbf{k}_{1BZ}$-point sampling does not affect the value of the physical quantity Q (typically Q may be the formation energy of a defect). A 1-dimensional example may clarify this aspect. Initially we choose a small super-cell with a real-space dimension a_{small} and containing a point defect. a_{small} is a single Bravais lattice vector meaning that the structure repeats itself with a period a_{small}. The corresponding

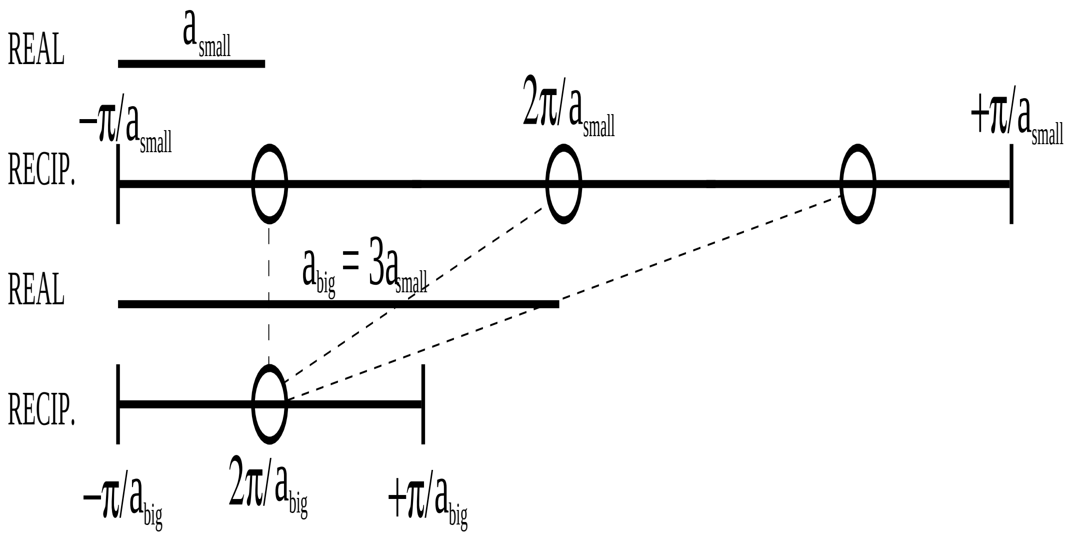

Figure 14: When increasing the size of the super-cell, the density of **k**-points in the first Brillouin zone should be kept constant, if one wants comparable results. The selected **k**-points are indicated by circles.

reciprocal lattice vector has length $\frac{2\pi}{a_{small}}$ (Fig. 4.5, two upper lines). The first BZ ranges from $\frac{-\pi}{a_{small}}$ to $\frac{+\pi}{a_{small}}$. We have selected three equidistant $\mathbf{k}_{1BZ}$-points in the first BZ. Let the next super-cell be three times larger in the real-space than the original one (Fig. 4.5, two lower lines), again with one point defect. In this case the repeat period is three times larger than with the smaller super-cell, *i.e.* $a_{big} = 3a_{small}$. Thus the length of the first BZ is one third of the previous one. In order to keep the sampling density constant in the reciprocal space, one needs with the larger super-cell only one third of the number of the $\mathbf{k}_{1BZ}$-points compared the smaller real-space super-cell. The positions of the **k**-points in different super-cells should be equivalent. This is achieved by applying folding operations when moving from the smaller real-space super-cell to a bigger one. In two dimensions and especially in three dimensions the situation is more difficult because the folding operations become more intractable.

5 Simulation results

5.1 Simulated measurement of Young's modulus of amorphous carbon (Pub. I)

As a part of a larger experimental study, molecular dynamics simulations regarding the possibility of measuring Young's modulus with a simulated atomic force microscope (AFM) measurement are made. A classical potential introduced by Tersoff is applied (Sec. 4.1). An AFM-tip of the order of 30 carbon atoms is pushed to different lateral positions of an *a-C* film. The force acting on the tip is recorded as the function of the indentation depth. It is found that the simulation result for the Young's modulus is very dependent on the initial lateral position of the AFM-tip. The simulated values range from 200 GPa to 600 GPa (experimentally 150-1000 GPa). We attribute the strong lateral dependence mainly to the deficiencies in the simulation model. The indentation depth is very small, about 0.3 nm, compared to experimental value of hundreds of nm. In the simulations, the tip shape is atomically sharp, whereas in reality the edge of the tip is flat over atomic dimensions. Also the elasticity assumption used in the equations to derive the Young's modulus is not valid in the simulations, because plastic deformations and mass transport between the tip and the surface sample are present.

5.2 Doping of bulk amorphous carbon (Pub. II)

Bulk samples of diamond and *a-C* are doped in order to examine the possibility of *n*-type doping of these materials. A first-principles approach with the DFT-LDA approach (Sec. 4.3) is selected because of the many different atomic species involved in the study. The formation energies of single substitutional atoms in various charge states are calculated. The set of atom species studied consists of nitrogen (N), oxygen (O) and chlorine (Cl). If substituted to the tetrahedral site (*i.e.* the substitute has four neighbors) N can donate one electron to a donor state, O can donate two and Cl three electrons. Nitrogen and oxygen have the lowest formation energies in diamond and in *a-C*. In *a-C* the preferable substitutional site is sp^2-coordinated. Chlorine has clearly highest formation energies in all studied cases. None of the studied dopants has shallow *n*-type donor states. The *n*-type shallow donor state is not found in this paper. However, the oxygen related states in *a-C* are not analyzed, which leaves the possibility of *n*-type doping with oxygen in a-C open.

5.3 Nitrogen doping of clean and hydrogenated diamond {100} and {111} surfaces (Pub. III)

In order to study whether the presence of a surface affects the behavior of a single substitutional nitrogen (N) atom in diamond a DFTB (Sec. 4.2) simulation is carried out. A single subsurface N atom is substituted in the vicinity of clean reconstructed diamond {100} and {111} surfaces. Moreover, the influence of hydrogen (H) termination of the surfaces on the N atom and associated electronic levels is studied.

It is found that, with the hydrogen termination, the situation is very similar to that in bulk diamond. The N atom moves to a trigonal configuration (sp^2-like) with the two remaining electrons occupying a lone-pair state. Additionally, a mid-gap state is formed. It is associated with the neighboring carbon atom with only three neighbors. On the contrary, with clean (unsaturated) diamond surfaces, the N atoms remain four-fold coordinated. The extra electron escapes to an anti-bonding state, which is localized on the surface. Thus this surface electron elongates some of the surface bonds. However, there is no n-type doping because the electron state associated to the surface electron does not bring a new state in the energy gap. The conclusion of this work is that the n-type doping of diamond is impossible with N in the vicinity of a diamond surface, as found earlier for bulk diamond.

5.4 The influence of boron and nitrogen doping on growth of CVD {100}:H diamond (Pub. IV)

Perhaps the commercially most successful technique to fabricate artificial diamond is the chemical vapor deposition (CVD) method. The kinetic growth model of CVD-diamond states that the growth parameter

$$\alpha = \frac{V_{100}}{V_{111}} \cdot \sqrt{3}$$

determines the shape of the growing diamond nucleus [69]. V_{100} and V_{111} are the growth rates on {100} and {111} surfaces. A qualitative argument states that the growth rate on one surface (for example V_{100}) should be much larger than on the other surfaces in order to grow single crystalline diamond with V_{100} surfaces. However, in practice, the growth rate is fastest on the {110} surface, typically about 3-5 times higher compared to the

{100} surface (growth rates on {111} surfaces are usually slightly higher than on {100}). The problem with CVD diamond is, even though it may be almost completely diamond and sp^3-bonded, the presence of domain boundaries between different crystal orientations. These extended defects cause problems especially in electronics applications, because they can trap electrons and thus reduce the number of current carriers. In order to obtain a more quantitative picture of the CVD-growth on diamond {100} surfaces, we investigate the growth model proposed by Harris and Goodwin [70]. The DFTB computational framework is employed (Sec. 4.2). In particular the effect of nitrogen and boron on diamond growth is studied. Our results suggest that the boron doping enhances the growth on the diamond {100} surface, and the growth can proceed with the Harris-Goodwin mechanism. On the contrary, N doping blocks the Harris-Goodwin pathway. Therefore we present a novel growth pathway in the case of N doping. The new reaction pathway requires less reaction steps as the earlier ones, and is therefore more likely to occur.

5.5 Nitrogen doping of amorphous carbon surfaces (Pub. V)

Amorphous carbon films have been proposed as candidates for flat electron emitting devices [20]. Similarly to diamond, there is experimental evidence of low or even negative electron affinity (NEA) in *a*-C films, especially in nitrogen doped *a*-C [14]. Because of NEA, electrons excited to the conduction band spontaneously escape to vacuum.

An *a-C* carbon surface is prepared starting with the bulk *a-C* sample generated earlier (Publication II). *Ab initio* methods with the DFT-LDA approach are utilized (Sec 4.3). The structural properties of the relaxed non-doped *a-C*-surface are compared to earlier studies. The agreement is found to be good. Nitrogen doping of the *a-C* surface is carried out using single N substitutions at different atomic environments. Furthermore, heavy N doping of 13% and 25% with different implantation profiles is studied. The aim of this study is to search for the explanation of the low electron affinity of the N doped *a-C* films. To accomplish this, work functions of different *a-C* surfaces with various N doping configurations are calculated. The work function is defined as the energy required to extract the most energetic electron on the surface (the Fermi electron) to the vacuum. The only doping configurations that reduce the electron affinity are the single substitutions on the top of the surface. This result explains the experimental discovery that with 0.4 at.-% nitrogen doping the electron affinity is at its minimum. With higher doping concentrations we find that the N atoms abstract from the surface as N_2 molecules.

5.6 Growth of amorphous carbon (Pub. VI)

Amorphous carbon layers can be fabricated using various methods (Sec. 3.2). However, a theoretical understanding of the growth even when using mono-energetic neutral carbon atoms is incomplete. There exist at least two contradicting theories on the subject. Lifshitz *et al.* suggest that the deposited atom penetrates into the subsurface region and an expansion of the film via stress relief results [71]. On the other hand Marks *et al.* propose that the new bonds form directly on top of the growing surface [72]. A different view is given by Koponen *et al.* They describe the deposition event as a two stage process. A high pressure and temperature peak immediately ($\lessapprox 30fs$) after the deposition event causes a densification in the film. The subsequent relaxation phase rearranges the surface atoms. The rearrangement continues until the temperature has dropped below 3000 K [73]. To study this subject at the atomic level in three dimensions, we perform a simulation where 600 single carbon atoms are deposited on the *a-C* surface with four different beam energies E_{beam} = 10 eV, 40 eV, 100 eV and 150 eV. A classical Tersoff potential is used (Sec. 4.1). Based on the simulation results we present a modified theory of the ion-beam induced growth of amorphous carbon. The growth of amorphous carbon proceeds on the surface at low energies ($E_{beam} \approx$ 10 eV). At higher energies, the growth is increasingly taking place in the subsurface region by global film expansion and single-atom diffusion towards the surface. The co-deposition with inert heavy ions with suitable kinetic energy might enhance the film quality, because it causes a many-atom diffusion into the subsurface direction. The growth rate is found to depend strongly on the implantation energy. It has a maximum at $E_{beam} \approx$ 40 eV, because the sputtering of the surface-atoms is still low at this energy, and the adsorption probability of the deposited atom has reached its maximum. The healing of the bonds after a deposition event requires at least 5 ps in amorphous material, which is much longer than earlier believed.

6 Summary

In this thesis the properties and growth of carbon-based materials were examined. For pure carbon *a-C* systems (Publications I and VI) a classical Tersoff potential was utilized. Two chemical vapor deposited (CVD)-diamond related simulations were carried out using the tight-binding method. Doping of amorphous carbon (*a-C*) was studied using *ab initio* techniques.

In three of the Publications, sort of 'negative' results were obtained. In Publication I the use of molecular dynamics in simulations of AFM measurements turned out to be too sensitive to local surface geometry in order to obtain macroscopic estimates for the Young's modulus of the surface. However, the recommendations of this paper were followed in a later publication with more general results [74]. In Publication II the search for *n*-type doping of diamond or *a-C* shows all candidates to have relatively deep levels or too high formation energies. The well-controlled *n*-type doping of *a-C* or diamond thus remains an open challenge. The search for *n*-type doping was performed also in Publication III. In this case CVD-diamond surfaces $\{100\}$ and $\{111\}$ were nitrogen doped. With hydrogen termination of these surfaces they behave like bulk diamond, resulting in off-site motion of the N atom and a mid gap electron state. With clean surfaces the extra electron from the tetragonal N-atoms escapes to the surface stretching some of the surface bonds. The associated electron energy states are again in the midgap region, so one fails to obtain *n*-type doping. Nevertheless, the surface bond elongation argument proved to be useful in a later study concerning surface diffusion precesses (Publication IV).

The last three Publications have, on the contrary, 'positive' results. In Publication IV a new pathway for diamond growth on hydrogenated and nitrogen doped diamond $\{100\}$ surfaces was proposed. This new pathway contains less energy barriers and less reactions than the ones suggested earlier. We also found that boron doping should enhance the growth rate on $\{100\}$ diamond and that the Harris-Goodwin reaction is valid. An explanation for the experimentally observed low electron affinity on amorphous carbon (*a-C*) was given in Publication V. We argued that the origin of the low electron affinity are the nitrogen atoms bonded on the very top of the *a-C* surface. In Publication VI the growth of *a-C* was studied in detail employing a classical Tersoff's potential. A compromise between the earlier growth models was suggested. Moreover, co-implantation with heavy ions was recommended with certain growth energies.

References

[1] J. Robertson, Advances in Physics, **35**, 317 (1986).

[2] J. Robertson and E. P. O'Reilly, Phys. Rev. B **35**, 2946 (1987).

[3] R. Ahuja, S. Auluck, J. Trygg, J. M. Wills, O. Eriksson and B. Johansson, Phys. Rev. B **51**, 4813 (1995).

[4] U. Stephan, T. Frauenheim, P. Blaudeck, and G. Jungnickel, Phys. Rev. B **49**, 1489 (1994).

[5] P. A. Schultz and E. B. Stechel, Phys. Rev. B **57**, 3295 (1998).

[6] N. A. Marks, D. R. McKenzie, B. A. Pailthorpe, M. Bernasconi, and M. Parrinello, Phys. Rev. B **54**, 9703 (1996).

[7] C. Cunha, S. Canuto, and A. Fazzio, Phys. Rev. B **48**, 17806 (1993).

[8] S. A. Kajihara, A. Antonelli, J. Bernholc, and R. Car, Phys. Rev. Lett. **66**, 2010 (1991).

[9] S. Pöykkö, M. Kaukonen, M. J. Puska, and R. M. Nieminen, Comp. Mat. Sci. **10**, 351 (1998).

[10] M. Nesládek, K. Meykens, K. Haenen, L. M. Stals, T. Teraji, and S. Koizumi, Phys. Rev. B **48**, 17806 (1993).

[11] P. Sitch, Th. Köhler, G. Jungnickel, D. Porezag, and Th. Frauenheim, Solid State Comm. **100**, 549 (1996).

[12] G. Jungnickel, P. Sitch, Th. Frauenheim, B. R. Eggen, M. I. Heggie, C. D. Latham, and C. S. G. Cousins, Phys. Rev. B **57**, R661 (1998).

[13] J. Robertson, Unpublished.

[14] B. S. Satyanarayana, A. Hart, W. I. Milne, and J. Robertson, Appl. Phys. Lett. **71**, 1430 (1997).

[15] M. Werner and R. Locher, Rep. Prog. Phys. **61**, 1665 (1998).

[16] J. F. Prins in *The Physics of Diamond:* proceedings of the International School of Physics "Enrico Fermi", Course CXXXV (IOS Press, Amsterdam, 1997), pp. 411-484.

[17] F. P. Bundy, Physica A **156**, 169 (1989).

[18] G. Galli, R. M. Martin, R. Car, and M. Parrinello, Phys. Rev. Lett. **63**, 988 (1989).

[19] A. Vescan, I. Daumiller, P. Gluche, W. Ebert, and E. Kohn, IEEE Trans. Electron. Devices Lett. **18**, 556 (1997).

[20] K. Okamo, S. Koizumi, S. R. P. Silva, and G. A. J. Amaratunga, Nature **381**, 140 (1996).

[21] L. K. Cheach, X. Shi, E. Liu, and J. R. Shi, Appl. Phys. Lett. **73**, 2473 (1998).

[22] E. G. Gerstner and D. R. McKenzie, J. Appl. Phys. **84**, 5647 (1998).

[23] G. Z. Cao, J. J. Schermer, J. P. van Enckevort, W. A. L. M. Elst, and L. J. Gilling, J. Appl. Phys. **79**, 1357 (1996).

[24] P. Bachmann, D. Leers, and H. Lydtin, Diam. Relat. Mater. **1**, 1 (1991).

[25] D. G. Goodwin, Appl. Phys. Lett. **59**, 277 (1991).

[26] M. Kamo, Y. Sato, S. Matsumoto, and N. Sekata, J. Cryst. Growth **62**, 642 (1983).

[27] S. Skokov, B. Weiner, and M. Frenklach, J. Phys. Chem. **98**, 7073 (1994).

[28] D. R. McKenzie, Rep. Prog. Phys. **59**, 1611 (1996).

[29] I. I. Aksenov, S. I. Vakula, V. G. Padalka, R. E. Strelnitski, and V. M. Khoroshikh, Sov. Phys. Tech. Phys. **25**, 1164 (1980).

[30] H. Lüth, *Surfaces and Interfaces of Solids* (Springer, Berlin, 1993).

[31] W. Müller-Sebert, E. Wörner, F. Fuchs, C. Wild, and P. Koidl, Appl. Phys. Lett. **68**, 759 (1996).

[32] J. Mort, D. Kuhlman, M. Morgan, F. Jansen, K. Okumura, Y. M. LeGrice, and R. J. Nemanich, Appl. Phys. Lett. **55**, 1121 (1989).

[33] J. F. Prince, Phys. Rev. B **38**, 5576 (1988).

[34] N. N. Greenwood and A. Earnshaw in *Chemistry of Elements* (Pergamon Press, Oxford, 1984), pp. 296-378.

[35] P. H. Gaskell, A. Saeed, P. Chieux, D. R. McKenzie, Phys. Rev. Lett. **67**, 1286 (1991).

[36] V. I. Merkulov, J. S. Lannin, C. H. Munro, S. A. Asher, V. S. Veerasamy, and W. I. Milne, Phys. Rev. Lett. **78**, 4869 (1997).

[37] H. Ibach and H. Lüth, *Solid-State Physics* (Springer, Berlin, 1995).

[38] R. Kalish, Y. Lifshitz, and S. Prawer, Appl. Phys. Lett. **74**, 2936 (1999).

[39] C. Arena, B. Kleinsorge, J. Robertson, W. I. Milne, and M. E. Welland, J. Appl. Phys. **85**, 1609 (1999).

[40] R. W. Robinett, *Quantum Mechanics* (Oxford University Press, Oxford, 1997).

[41] G.M. Pharr, W.C. Oliver, F.R. Brotzen, J. Mater. Res. **7**, 613 (1992).

[42] D. M. Schaefer, A. Patil, R. P. Andres, and R. Reifenberger Phys. Rev. B **51**, 5322 (1995).

[43] M. C. Payne, M. P. Teter, D. C. Allan, T. A. Arias, and J. D. Joannopoulos, Rev. Mod. Phys. **64**, 1045 (1992).

[44] R. O. Jones and O. Gunnarsson, Rev. Mod. Phys. **61**, 689 (1989).

[45] P. Hohenberg and W. Kohn, Phys. Rev. **136**, B864 (1964).

[46] W. Kohn and L. J. Sham, Phys. Rev. **140**, A1133 (1965).

[47] N. W. Ashcroft and N. D. Mermin, *Solid State Physics* (CBS Publishing Asia, Hong Kong, 1988), pp. 334-337.

[48] J. C. Slater, *Quantum Theory of Atomic Structure* (McGraw Hill, New York, 1960).

[49] P. P. Ewald, Ann. Phys. (Leipzig) **64**, 253 (1921).

[50] M. Fuchs and M. Scheffler, submitted to Computer Physics Communications (1999).

[51] V. Sammalkorpi, *A 3d-active Pseudopotential for Gallium*, Special Assignment, Laboratory of Physics, Helsinki University of Technology (1999).

[52] C. M. Goringe, D. R. Bowler and E. Hernándes, Rep. Prog. Phys. **60**, 1447 (1997).

[53] G. Seifert and H. Eschrig, Phys. Status Solidi B **127**, 573 (1985).

[54] D. Porezag, Th. Frauenheim, Th. Köhler, G. Seifert, and R. Kaschner, Phys. Rev. B **51**, 12947 (1995).

[55] J. C. Slater and G. F. Koster, Phys. Rev., **94**, (1954) 1498.

[56] M. Elstner, D. Porezag, G. Jungnickel, J. Elsner, M. Haugk, Th. Frauenheim, S. Suhai, and G. Seifert, Phys. Rev. B **58**, (1998) 7260.

[57] J. Tersoff, Phys. Rev. B **37**, 6991 (1988).

[58] D. W. Brenner, Phys. Rev. B **42**, 9458 (1990).

[59] N. A. Marks, D. R. McKenzie, and B. A. Pailthorpe, Phys. Rev. Lett. **76**, 768 (1996).

[60] J. Tersoff, Phys. Rev. Lett. **61**, 2879 (1988).

[61] W. H. Press, B. P. Flannery, S. A. Teukolsky, and W. T. Vetterling, *Numerical Recipes*, (Cambridge University Press, Cambridge, 1989).

[62] G. T. Barkema and N. Mousseau, Phys. Rev. Lett. **77**, 4358 (1996).

[63] N. Mousseau and G. T. Barkema, Phys. Rev. E **57**, 2419 (1998).

[64] M. I. Dykman, P. V. E. McClintock, V. N. Smelyanski, N. D. Stein, and N. G. Stocks, Phys. Rev. Lett. **68**, 2718 (1992).

[65] D. Frenkel and B. Smit, *Understanding Molecular Simulation* (Academic Press, San Diego, 1996).

[66] H. J. C. Berendsen, J. P. M. Postma, W. F. van Gunsterer, A. DiNola, and H. R. Haak, J. Chem. Phys. **81**, 3684 (1984).

[67] S. Froyen, Phys. Rev. B **39**, 3168 (1989).

[68] H. J. Monkhorst and J. D. Pack, Phys. Rev. B **13**, 5188 (1976).

[69] C. Wild, P. Koidl,W. Müller-Sebert, H. Walcher, R. Kohl, N. Herres, R. Locher, R. Samlenski, and R. Brenn, Diam. Rel. Mat. **2** , 158 (1993).

[70] S. J. Harris and D. G. Goodwin, J. Phys. Chem. **97**, 23 (1993).

[71] Y. Lifshitz, S. R. Kasi, and J. W. Rabalais, Phys. Rev. Lett. **62**, 1290 (1989).

[72] N. A. Marks, D. R. McKenzie, and B. A. Pailthorpe, Phys. Rev. B **53**, 4117 (1996).

[73] I. Koponen, M. Hakovirta, and R. Lappalainen, J. Appl. Phys. **78**, 1 (1995).

[74] R. Astala, M. Kaukonen, T. Heine, and R. M. Nieminen, accepted to Phys. Rev. B. (1999).